Journal of Sound and Vibration 329 (2010) 2716–2737

Contents lists available at ScienceDirect

Journal of Sound and Vibration

journal homepage: www.elsevier.com/locate/jsvi

Active control of a piezo-composite rotating beam using coupled plant dynamics

N.K. Chandiramani [*]

Department of Civil Engineering, Indian Institute of Technology Bombay, Mumbai 400076, India

A R T I C L E I N F O

Article history:
Received 29 May 2009
Received in revised form
21 December 2009
Accepted 22 January 2010
Handling Editor: D.J. Wagg
Available online 26 February 2010

A B S T R A C T

Optimal control of a thin-walled rotating beam is considered using a higher-order shear deformation theory (HSDT). The beam is pretwisted, doubly tapered, and carries a tip rotor. It comprises an orthotropic host with surface-embedded transversely isotropic piezoelectric sensor-actuator pairs. Spanwise and thicknesswise variation of the electric field applied to actuators is considered. This yields a coupled electro-mechanical system, wherein all displacement variables are coupled via the electric field. Hence, coupling between bending-transverse shear and extension-twist occurs even when the ply angle configuration has circumferentially uniform stiffness. Optimal LQR control with state feedback is used to obtain the control input, i.e., charge density (hence voltage) applied to actuators. Parametric studies involving ply-angle, rotation speeds of beam and rotor, pretwist, taper, rotor mass, and saturation constraint on actuator voltage, are performed. The HSDT yields lowest coupled natural frequencies (as compared to unshearable and first-order shear models) thus providing conservative data, useful for passive and active control designs. The present plant model, with spanwise varying electric field, yields an order-of-magnitude reduction in settling time and control voltage, and lower response, vis-a-vis the decoupled approach.

1. Introduction

Fiber-reinforced composites with embedded piezoelectric elements provide a means for synthesis of passive and active control. Their common application is in aerospace structures requiring precise control. This is often realized by optimal controller design that yields reduced settling time and control energy. Such designs require an accurate plant model that incorporates electromechanical coupling, transverse shearability, satisfaction of traction free boundary conditions (BCs), warping restraint, etc.

Kim and White [1] analyzed a non-rotating thick-walled beam using a cubic variation of axial displacements to satisfy traction free BCs. Their results correlated well with available experimental results for both symmetric and antisymmetric layups. Eigenvibrations for various rotating beam configurations have been widely researched. Rosen et al. [2] studied pretwisted blading using non-physical coordinates and untwisted eigenvibration modes to de-couple the two plane bending. Jung et al. [3] used the first-order shear deformation theory (FSDT) and a mixed variational approach with plane stress constitutive relations. They obtained results showing a pronounced effect of wall thickness and first-order transverse shear on eigenvibrations. Song et al. [4] considered the FSDT for eigenvibration control of pretwisted blades with piezoactuators. They used either proportional or velocity feedback for control moments and studied the effect of pretwist.

---

[*] Tel.: +91 22 25767311; fax: +91 22 25767302.
E-mail addresses: naresh@civil.iitb.ac.in, nareshkc@iitb.ac.in.

0022-460X/$ - see front matter © 2010 Elsevier Ltd. All rights reserved.
doi:10.1016/j.jsv.2010.01.023

Nomenclature

a^p_{ij}, $\tilde{a}^p_{ij}$, $a_{ij}[z]$, $\tilde{a}_{ij}[z]$	global stiffnesses (untwisted, HSDT, pretwist, HSDT with pretwist)
a_{Pi}, L_{Pij}	global piezoelectric coefficients
$\mathcal{A}_s$, $\mathcal{S}_s$	actuator and sensor patch distribution, respectively
$2b_{\text{tip}}$; $2b_{\text{root}}$	tip depth; root depth
C^P_{ij},ρ^P	3-D elastic constants, mass density of piezopatch
C_P, A_P,t_P, 2κ	capacitance, surface area, thickness, and width of piezopatch, respectively
e_{ij}, $\mathcal{E}_{ij}$	piezoelectric, reduced piezoelectric constants of piezopatch
$\overline{\mathcal{E}}_{ij}$	reduced piezoelectric coefficients of smart composite beam
E_i; D_i	electric field vector; electric displacement vector
E^H_i,G^H_{ij}, ν^H_{ij}, ρ^H	Youngs moduli, shear moduli, Poisson's ratios, density of orthotropic host
f_s, f_z, f_n	distribution of piezopatches in s-, z-, n-direction, respectively
F_ω, a	primary and secondary warping function, respectively
$\tilde{\mathcal{H}}$; $\mathbf{R}$; $\mathbf{R}_R$	electric enthalpy; beam position vector; rotor position vector
$(\mathbf{I},\mathbf{J},\mathbf{K})$; $(\mathbf{i},\mathbf{j},\mathbf{k})$; $(\mathbf{i}_R\mathbf{j}_R, \mathbf{k}_R)$:]	inertial-fixed basis; beam-fixed bases; rotor-fixed bases
$(I_1,\ldots,I_9,I^p_{xx},I^p_{yy},I^p_{\omega\omega},\hat{I}_P)$; b_1	structural inertia quantities; mass per unit length of beam
I_{zz}, I_{xxyy}	polar, inplane mass moment of inertia of tip rotor
L, $2b$, $2c$, h	span, depth, width, and wall thickness, respectively, of beam
m^p, l^p	direction cosines between local principal- and local surface-coordinate directions
$\mathbf{M}$; $\mathbf{G}$; $\mathbf{K}$	mass matrix; gyroscopic matrix; stiffness matrix
$\mathbf{M}_{ij}$; $\mathbf{m}_{ij}$	submatrices of mass matrix due to beam; due to tip rotor
N; $\mathbf{\Phi_i}$, $\mathbf{q_i}$	number of trial functions; N-dimensional vectors of trial functions, generalized coordinates
$p_y[z,t]$; p_m	applied line load in y-direction; initial value of applied uniform line load
$\mathbf{P}$; $\hat{\mathbf{G}}$, $\tilde{\mathbf{G}}$	Riccati matrix; state feedback gain for control voltage, charge density
$\tilde{q}_{Pi}$; $\mathbf{C}_i$	surface charge generated on sensors; associated discretization matrix
$\mathbf{Q}$; $\mathbf{F}$	external excitation vector; piezoelectrically induced forcing coefficient vector
Q^P_{ij}	reduced stiffness of piezopatch
$\overline{Q}^H_{ij}$	transformed reduced stiffness of host
$\overline{Q}_{ij}$	transformed reduced stiffnesses of smart composite beam
R_0	hub radius
$R[z]$	spanwise variation of axial (centrifugal) force
(s, n)	local cross-section surface coordinates (tangential-, normal- to mid-surface)
u, v, w	lag, flap, and axial (warping) displacement, respectively
u, I, P	control voltage, current, and power required, respectively
u_o, v_o, w_o, ϕ, θ_x, θ_y	displacement field (lag, flap of point $o(0,0)$, axial, twist, x- and y-rotations)
v^*	nondimensional flap response at beam tip
$V_{\max}$	actuator saturation voltage
$w_c[z;t]$	axial displacement of $C(x_c,y_c)$ lying on positive x^p axis
$\overline{w}$, $\overline{\gamma}_{sz}$	mid-contour axial displacement and shear strain
$\mathbf{x}$; $\mathbf{A}$; $\mathbf{B}$; $\mathbf{W}$	state; state matrix; control input matrix; excitation input matrix
(x, y, z); $(\overline{x},\overline{y})$	beam-fixed coordinates; corresponding mid-contour quantities
(x^p, y^p, z^p); $(\overline{x}^p,\overline{y}^p)$	local cross-section principal coordinates; corresponding mid-contour quantities
$\mathbf{Z}$; $\mathbf{R}$; α, μ, η	state weighting matrix; control input weighting matrix; corresponding weights
β; β_0; β_1, β_2	pretwist; linear coefficient; quadratic coefficients of pretwist
$(\gamma_{xz},\gamma_{yz})$; $(\overline{\gamma}_{xz},\overline{\gamma}_{yz})$	transverse shear strains and their mid-contour counterparts
δ_e, δ_t, δ_h	tracers for classical, FSDT, and HSDT formulation, respectively
$(\varepsilon_{ss},\varepsilon_{zz},\gamma_{sz},\gamma_{nz},\gamma_{ns})$	strain components in surface coordinates
$(\varepsilon_{xx},\varepsilon_{yy},\gamma_{xy})$	inplane strains
ξ_{ij}, ζ_{ij}	dielectric, reduced dielectric constants of piezopatch
ρ; ρ_R	mass density of beam and rotor, respectively
$(\sigma_{ss},\sigma_{zz},\tau_{sz},\tau_{nz},\tau_{ns})$	stress components in surface coordinates
σ; $2c_{\text{tip}}$; $2c_{\text{root}}$	taper ratio; tip width; root width
$\overline{\sigma}$; $\hat{\sigma}$	applied surface charge density; corresponding time dependency vector
ψ; ψ_o	electric potential; spanwise variation of potential
Ω; θ; ω_i	angular speed of hub/beam; ply-angle; natural frequency
$\overline{\Omega}$, m_R, k_R, r_m	angular speed, mass, polar radius of gyration, offset, of tip rotor

Yoo et al. [5] analyzed eigenvibrations of a pretwisted blade (arbitrarily oriented at the hub) carrying a tip mass. They retained gyroscopic effects and used hybrid deformation variables to linearize the system. Banerjee et al. [6] used the dynamic stiffness method in conjunction with the Wittrick–Williams algorithm to obtain natural frequencies of rotating, linearly tapered, unshearable beams.

Fazelzadeh and Hosseini [7] considered a FSDT model of a pretwisted, thin-walled, rotating FGM beam under aerothermoelastic loading with through-thickness temperature gradients. They used first-order piston theory aerodynamics, and gas dynamics theory for surface temperature. The solution obtained via extended Galerkin method showed a softening behavior with increasing Mach, number. Fazelzadeh et al. [8] obtained similar results using the differential quadrature method. Lee et al. [9] analyzed the inplane (bending-extension) free vibration of an unshearable, rotating curved beam with an elastically restrained root. A softening behavior with increasing speed, leading to divergence instability, was obtained for large values of the arc angle. Subsequently Lee et al. [10] obtained divergence instability for a rotating Timoshenko blade when the precone is large. Mei [11] used the differential transformation technique for flap mode analysis of a rotating unshearable beam and obtained eigensolutions in close agreement with available results.

Active control studies on rotating beams are comparatively fewer. Kunz [12] analyzed a saturation controller via perturbation and numerical methods, and found it effective in reducing tip responses even at moderately high rotation speeds and despite significant intermodal coupling. Choi et al. [13] considered a thin-walled, composite blade with PVDF sensors and piezoelectric fiber actuators (i.e., macro-fiber composites MFCs) and retained the Coriolis effect. Negative velocity feedback was used, although they proposed optimal control for future studies. The work was extended for pretwisted blades in [14]. Wei et al. [15] presented experimental results on control of an angular-accelerating sandwich-beam comprising an ER fluid core with aluminium surface layers. They proposed an optimal controller design for future studies. Cai and Lim [16] designed an optimal tracking controller for inplane motions of a flexible hub-beam system. A simplified first-order approximation coupling model that neglects axial deformation effect was used. Subsequently in [17] they included damping due to beam material, air, and hub bearing, and obtained results for damped passive response. Shete et al. [18] studied the optimal control of a pretwisted, composite, rotating beam with distributed piezoelectric sensors/actuators. Both classical and instantaneous optimal control methods were used. Significant eigenfrequency enhancements during structural tailoring via the HSDT model were reported. Lin [19] designed a PD controller using piezoelectric sensing and actuation for a rotating, unshearable beam with elastically restrained root. An uncoupled electromechanical model was considered in [18,19].

Pietrzakowski [20] considered the inplane variation of electric potential for velocity feedback control of a plate with piezoelectric sensors/actuators. An increase in plate stiffness was reported due to the coupling. Narayanan and Balamurugan [21] developed a Timoshenko laminated-beam finite element model with distributed piezoelectric sensors/ actuators. Results using velocity feedback, Lyapunov feedback, and LQR optimal controller designs showed that LQR design was most control effective and required least actuation voltage. Similar conclusions were obtained by Vasques and Rodrigues [22] when comparing constant gain and constant amplitude velocity feedback with the LQR and LQG methods, within a coupled electromechanical formulation.

Passive unimodal damping with shunted piezoelectrics was first demonstrated by Hagood and Flotow [23]. For resonant shunting, the circuit comprising series inductor–resistor shunt and piezoelectric capacitance is tuned to the structural resonance frequency of the mode to be damped, i.e., electrical resonance is tuned to the structural resonance. However, large inductors are required to produce low-frequency electrical resonance. Andreaus et al. [24] obtained efficient passive control of multimodal vibrations by interconnecting distributed piezoelectric bender transducers, embedded along beam length, via a synthesized passive electrical circuit analog of a Timoshenko beam along with resistive elements for dissipation. Resistor placements are optimized by either maximizing the decay rate or minimizing the strain energy time envelop. Thus, the electrical dissipative circuit provides multiresonance coupling with mechanical modes as well as optimal electrical dissipation of mechanical energy.

Multimode shunt design whereby shunt impedance is obtained from an effective feedback controller is discussed in Moheimani and Fleming [25]. The design of active shunt impedance using optimal controllers like LQG is also considered therein to overcome the limitation posed by large inductor requirements. Guyomar et al. [26] proposed a semi-passive control method termed synchronized switch damping, whereby piezoelements are in an open circuit for the most part except when a statistically evaluated threshold for deflection (or voltage) is reached, at which time a switch is triggered to invert the voltage. However, damping was found to decrease with increase in excitation frequency. The active shunting method in [25] and multimodal control in [24] hold great potential for implementation and further research. The LQR active control method considered herein is without shunting. It minimizes a performance index comprising the conflicting combination of mechanical energy and control input energy. This procedure, as is well known, yields increased gain margins and phase margins which result in reduced settling time and overshoot [15–17,21,22].

Optimal piezoelectric sensor/actuator placement and sizing using genetic algorithms is fast gaining interest among researchers. Han and Lee [27] sequentially used controllability and observability criteria with spillover prevention. Significant plate vibration reduction was observed for the first three modes using coupled positive position feedback during experimental validations. Dhuri and Sheshu [28] considered a multi-objective GA optimization to obtain minimum change in natural frequency (due to piezopatches) and good controllability for a rotating beam.

In [18,19,21,29] it is assumed that electric potential varies only through the thickness of the piezopatch, in a linear manner. This implies that electric field developed has zero inplane components and a spatially constant thickness-wise component that is proportional to applied voltage. This results in decoupling of the electromechanical system wherein controller design does not involve solution of charge equation. The present work discards this assumption by also considering the spanwise variation of the electric potential. This leads to a fully coupled electromechanical system where the charge equation is solved for controller design. Further, this also results in a coupling of all mechanical field variables (hence vibration modes), even for the special ply layup considered in [18] wherein this full coupling was absent, i.e., in [18] a decoupling occurs of bending—transverse shear motion on one hand and extension—twist motion on the other. The effect of taper (present in rotor blade designs) and tip rotor (resulting in gyroscopic forces) were not included in [18]. Herein, a HSDT model for pretwisted, composite blades is considered. The model formulation includes a tip rotor, double-taper, and spanwise distributed piezoelectric sensor/actuator pairs with electromechanical coupling considered. Optimal LQR design with state feedback is used to obtain the control input to actuators. Influence of electromechanical coupling, shear deformation, pretwist, taper, and the tip rotor are assessed.

2. Electro-mechanical system equations

Consider a straight beam, of span L, rigidly mounted on a rigid hub of radius R_0 (Fig. 1). The beam-hub system rotates with constant angular velocity $\Omega\mathbf{J}=\Omega\mathbf{j}$ about the fixed-in-space longitudinal axis $A-A$ of the hub. The beam has a hollow, single celled, rectangular cross-section with uniform wall thickness h, width $2c$, and depth $2b$ (Fig. 2). The cross-section is doubly tapered such that its width to depth ratio remains constant along the span. The taper ratio is defined as $\sigma=c_{\text{tip}}/c_{\text{root}}=b_{\text{tip}}/b_{\text{root}}$. Actuator and sensor patches, each of thickness t_P and width 2κ, are embedded on the top and bottom surface of the beam, respectively (Fig. 2). A pretwist $\beta[z]$ exists with either $\beta[z]=\beta_0 z/L$ or $\beta[z]=\beta_1 z/L+\beta_2(z/L)^2$ defining linearly or quadratically varying pretwist, respectively.

A tip rotor of mass m_R, polar radius of gyration k_R, is attached at an offset r_m from beam tip, and spins with constant angular velocity $\overline{\Omega}\mathbf{k}_R$, where $(\mathbf{i}_R,\mathbf{j}_R,\mathbf{k}_R)$ define the rotor fixed bases. The inertial fixed coordinate system (X, Y, Z) with bases $(\mathbf{I},\mathbf{J},\mathbf{K})$ originates at the hub center O, while the beam-fixed coordinate system (x, y, z) with bases $(\mathbf{i}, \mathbf{j}, \mathbf{k})$ originates at the beam root (i.e., point of attachment of beam to hub). Each cross-section contains two local coordinate systems, i.e., (s, n, z)

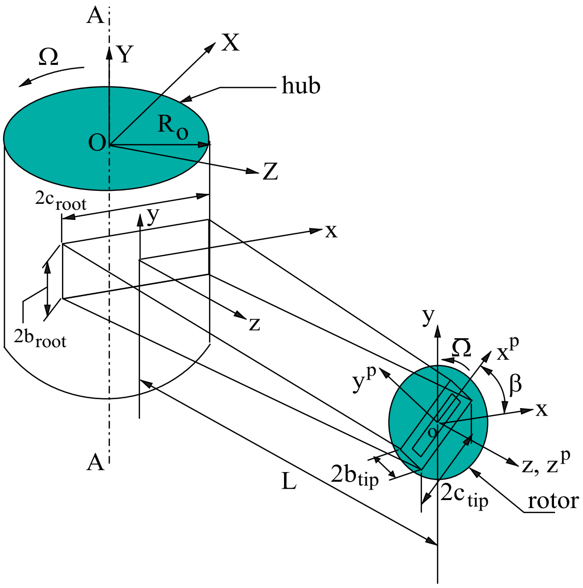

Fig. 1. Pretwisted tapered beam with tip rotor.

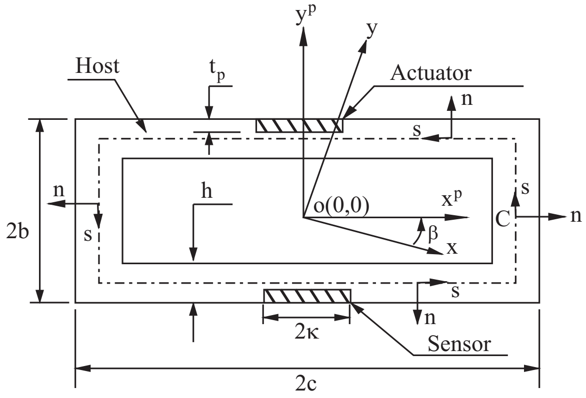

Fig. 2. Cross-sectional view and coordinate system.

surface coordinates, and (x^p, y^p, z^p) coordinates along the cross-section principal axes. For a point lying on the cross-section mid-contour (n=0), using overbars (¯) to denotes mid-contour quantities, the beam fixed coordinates are related to the sections principal axes coordinates as

$$\bar{x}[s,z]=\bar{x}^p[s]\cos\beta-\bar{y}^p[s]\sin\beta,\quad \bar{y}[s,z]=\bar{x}^p[s]\sin\beta+\bar{y}^p[s]\cos\beta,\quad z[s]=z^p \tag{1}$$

2.1. Kinematics

The assumptions adopted are: (1) $w \ll u$, $w \ll v$, where u (lag), v (flap), and w (axial/warping) denote displacements in the x, y, and z directions, respectively. Hence, nonlinearity involving the axial displacement is neglected. (2) Spanwise dependent rate of twist, i.e., $\phi' \equiv \phi'[z]$, in order to model the effect of warping restraint. (3) Quadratic variation of transverse shear strains γ_{xz} and γ_{yz} through wall thickness, in order to satisfy traction free BCs on upper and lower bounding faces ($n=\pm h/2$) of the generally orthotropic beam wall. (4) Secondary warping effect for points off the mid-contour is incorporated. (5) No in-plane cross-sectional distortion occurs (i.e., $\varepsilon_{xx}=\varepsilon_{yy}=\gamma_{xy}=0$). (6) Torsional shear strain along mid-contour pertains to a s-wise constant shear flow for a closed contour. (7) Ratio of wall thickness to wall radius of curvature is very small compared to unity (and exactly zero for cross-sections composed of linear segments). Hence, direction cosines of the normal $\mathbf{n}$ are expressible as $l^p(=x^p_{,n}=\mathrm{d}\bar{y}^p/\mathrm{d}s)\approx y^p_{,s}$ and $m^p(=y^p_{,n}=-\mathrm{d}\bar{x}^p/\mathrm{d}s)\approx -x^p_{,s}$. (8) σ_{nn} is negligible in the constitutive law.

Using assumption (5) and Eq. (1) the $u[x,y,z,t]$ and $v[x,y,z,t]$ displacements of a cross-section point are related to the corresponding displacements $u_o[z;t]$ and $v_o[z;t]$ of the (arbitrary) reference point $o(0,0)$, (Fig. 2), and the (small) twist $\phi[z;t]$ measured about the z axis, as [18]

$$u=u_o-(\bar{y}^p m_\beta+\bar{x}^p l_\beta)\phi-n(m^p m_\beta+l^p l_\beta)\phi,\quad v=v_o+(\bar{x}^p m_\beta-\bar{y}^p l_\beta)\phi+n(l^p m_\beta-m^p l_\beta)\phi \tag{2}$$

Here $m^p=-\mathrm{d}\bar{x}^p/\mathrm{d}s$ and $l^p=\mathrm{d}\bar{y}^p/\mathrm{d}s$ are direction cosines of (s, n, z) axes referred to (x^p, y^p, z^p) axes; and $m_\beta=\cos\beta$ and $l_\beta=\sin\beta$. The in-plane strains (using assumption (1)) and transverse shear strains (using assumption (3)) are

$$\varepsilon_{xx}=u_{,x}+0.5(u_{,x}^2+v_{,x}^2),\quad \varepsilon_{yy}=v_{,y}+0.5\left(u_{,y}^2+v_{,y}^2\right),\quad \gamma_{xy}=(u_{,y}+v_{,x}+u_{,x}u_{,y}+v_{,x}v_{,y}) \tag{3a}$$

$$\gamma_{xz}[z,n;t]=\bar{\gamma}_{xz}[z;t]+n\eta_x[z;t]+n^2\zeta_x[z;t],\quad \gamma_{yz}[z,n;t]=\bar{\gamma}_{yz}[z;t]+n\eta_y[z;t]+n^2\zeta_y[z;t] \tag{3b}$$

The stress–strain relations (expressed in the (s,n,z) system) for a generally orthotropic material are employed and the traction-free boundary conditions are imposed (i.e., $\tau_{ns}=\tau_{nz}=\sigma_{nn}=0$ at $n=\pm h/2$) with Eqs. (3b), assumptions (5, 8), and kinematic compatibility being considered. This results in a parabolic variation for the transverse shear strains, i.e.,

$$\gamma_{xz}=(1-4n^2/h^2)\bar{\gamma}_{xz}[z;t],\quad \gamma_{yz}=(1-4n^2/h^2)\bar{\gamma}_{yz}[z;t] \tag{4}$$

This is the essence of the HSDT considered here. The overbars (¯) on displacement and strain terms denote cross-section mid-contour quantities.

The axial (warping) displacement $w[x,y,z,t]$ is derived using shear strains. First $\bar{\gamma}_{sz}$ is expressed as the sum of bending shear strains γ_{xz}, γ_{yz} (using their parabolic form with n=0 and coordinate transformation) and torsional shear strains based on constant shear flow (assumption (6)). This is equated to the strain–displacement representation of $\bar{\gamma}_{sz}$ in terms of mid-contour displacement. Using assumption (7) and Eq. (2) in the resulting expression and then integrating it over the closed mid-contour, while requiring continuity of w, yields the torsional shear flow and $\bar{w}_{,s}$. Similarly γ_{nz} is expressed in terms of bending shear strains (torsional shear flow does not contribute) and equated to its strain–displacement representation to yield $w_{,n}$ after using assumption (7) and Eq. (2). Finally, starting from a conveniently chosen mid-contour origin $C(x_c,y_c)$ (taken to lie on the positive x^p axis for the box-beam) and integrating $\bar{w}_{,s}$ with respect to s, and then integrating $w_{,n}$ with respect to n in the interval [0, n], one obtains [18]

$$\begin{aligned}w=w_o-(F_\omega[s]+na[s])\phi'-\delta_h\frac{4n^3}{3h^2}\left[(u_o'-\theta_y)(l^p m_\beta-m^p l_\beta)+(v_o'-\theta_x)(m^p m_\beta+l^p l_\beta)\right]+\left(\left[\bar{x}^p+nl^p\right]l_\beta\right.\\ \left.+\left[\bar{y}^p+nm^p\right]m_\beta\right)(\delta_t\theta_x-\delta_e v_o')-\left(\left[\bar{x}^p+nl^p\right]m_\beta-\left[\bar{y}^p+nm^p\right]l_\beta\right)(\delta_t\theta_y+\delta_e u_o')\end{aligned} \tag{5}$$

where

$$\theta_y[z;t]=u_o'-\bar{\gamma}_{xz},\quad \theta_x[z;t]=-v_o'+\bar{\gamma}_{yz},\quad r_n[s]=\bar{x}^p\frac{\mathrm{d}\bar{y}^p}{\mathrm{d}s}-\bar{y}^p\frac{\mathrm{d}\bar{x}^p}{\mathrm{d}s},\quad \psi=\frac{\oint r_n\,\mathrm{d}s}{\oint \mathrm{d}s}$$

$$a[s]=-\bar{x}^p\frac{\mathrm{d}\bar{x}^p}{\mathrm{d}s}-\bar{y}^p\frac{\mathrm{d}\bar{y}^p}{\mathrm{d}s},\quad F_\omega=\int_0^s(r_n-\psi)\,\mathrm{d}s^*,\quad w_o[z;t]=w_c-y_c\theta_x+x_c\theta_y \tag{6}$$

Here $(')=\mathrm{d}()/\mathrm{d}z$; $w_c[z;t]$ is the axial displacement of point C; $\theta_x[z;t]$ and $\theta_y[z;t]$ are rotations about x and y axes, respectively; $F_\omega[s]$ and $a[s]$ are primary and secondary warping functions, respectively. Tracers ($\delta_e,\delta_t,\delta_h$) assume values (1,0,0), (0,1,0) and (0,1,1) when considering the beam as unshearable, first-order shearable and higher-order shearable, respectively. Hence, the displacement field variables are $u_o[z;t]$, $v_o[z;t]$, $\theta_x[z;t]$, $\theta_y[z;t]$, $w_o[z;t]$, and $\phi[z;t]$.

2.2. Piezopatch distribution, electric field

The transversely isotropic PZT-4 sensor and actuator patches are embedded on the bottom and top face, respectively. Their surface of isotropy is parallel to the mid-surface of the pretwisted beam (Fig. 2). They are distributed as

$$f_s = \underbrace{\mathcal{H}[s-b-c+\kappa]-\mathcal{H}[s-b-c-\kappa]}_{\mathcal{A}_s} + \underbrace{\mathcal{H}[s-3b-3c+\kappa]-\mathcal{H}[s-3b-3c-\kappa]}_{\mathcal{S}_s} \tag{7a}$$

$$f_z = \sum_{i=1}^{\mathcal{P}} (\mathcal{H}[z-z_i^-]-\mathcal{H}[z-z_i^+]), \quad f_n = \mathcal{H}[n-h/2+t_P]-\mathcal{H}[n-h/2] \tag{7b}$$

where f_s, f_z, and f_n are functions defining the piezopatch distribution in the s, n, and z directions, respectively. Here $\mathcal{H}$, $\mathcal{A}_s$, and $\mathcal{S}_s$ denote the Heaviside, actuator, and sensor distributions, respectively, and $\mathcal{P}$ is the number of collocated sensor–actuator pairs along the beam length. The electric potential distribution is assumed to be linear through the thickness of the actuator patch [20,21]. This amounts to discarding the shear-like electrical effect [30]. Considering the piezopatch to be grounded at the interface with the laminate substrate, the electric potential distribution can be written as $\psi[s,n,z,t] = \hat{n}\psi_o[z,t]$ where $\hat{n} = n-h/2+t_P$. Thus the electric field due to applied control voltage on the actuator is,

$$E_1 = -\partial\psi/\partial s = 0, \quad E_2 = -\partial\psi/\partial z = -\hat{n}\psi_o', \quad E_3 = -\partial\psi/\partial n = -\psi_o[z,t] \tag{8}$$

Thus, the electric field is nonuniform in the spanwise direction. This yields a fully coupled electromechanical system as discussed below.

2.3. Constitutive relations

Using assumption (8), the reduced constitutive law for orthotropic (graphite-epoxy) host and transversely isotropic piezopatches (PZT-4) are written [4]. Hence the stress–strain relation for a constituent piezocomposite beam-wall layer is expressed as

$$\begin{Bmatrix} \sigma_{ss} \\ \sigma_{zz} \\ \tau_{sz} \end{Bmatrix} = \begin{bmatrix} \overline{Q}_{11} & \overline{Q}_{12} & \overline{Q}_{16} \\ \overline{Q}_{12} & \overline{Q}_{22} & \overline{Q}_{26} \\ \overline{Q}_{16} & \overline{Q}_{26} & \overline{Q}_{66} \end{bmatrix} \begin{Bmatrix} \varepsilon_{ss} \\ \varepsilon_{zz} \\ \gamma_{sz} \end{Bmatrix} - \begin{Bmatrix} \overline{\mathcal{E}}_{31}E_3 \\ \overline{\mathcal{E}}_{31}E_3 \\ 0 \end{Bmatrix}, \quad \begin{Bmatrix} \tau_{nz} \\ \tau_{ns} \end{Bmatrix} = \begin{bmatrix} \overline{Q}_{44} & \overline{Q}_{45} \\ \overline{Q}_{45} & \overline{Q}_{55} \end{bmatrix} \begin{Bmatrix} \gamma_{nz} \\ \gamma_{ns} \end{Bmatrix} - \begin{Bmatrix} \overline{\mathcal{E}}_{15}E_2 \\ 0 \end{Bmatrix} \tag{9}$$

where $\overline{Q}_{ij}$ and $\overline{\mathcal{E}}_{ij}$ are transformed reduced stiffnesses and reduced piezoelectric coefficients, respectively, of the composite beam (Appendix A). The 3-D constitutive equations are reduced to a 1-D dependency via strain–displacement relations and integration over the cross-section (i.e., first through the thickness and then over the mid-contour).

In this regard it should be noted that Maurini et al. [30] used equivalent-single-layer Euler–Bernoulli kinematics to study a layered piezocomposite beam. Layerwise linear distributions for plane stresses (with zero shear) and electric potential, and layerwise constant electric displacement, is assumed. Zero transverse inplane stress resultants are imposed. The cross section remains normal to the beam axis but is allowed to deform in its own plane. The model predicts electromechanical constitutive coefficients accurately even when thickness of piezolayers is comparable to that of elastic ones. As compared to the Euler–Bernoulli formulation in [30], the present formulation accounts for inplane and transverse shear stresses, but without permitting inplane cross-sectional distortion (i.e., assumption (5)).

2.4. Governing system

Hamiltons principle for the beam with rotor reads [31,4],

$$\int_{t_0}^{t_1} \left[\int_\tau (\delta\tilde{\mathcal{H}} + \rho\ddot{\mathbf{R}}\cdot\delta\mathbf{R})\,\mathrm{d}\tau + \int_{\tau_R} (\rho_R \ddot{\mathbf{R}}_R \cdot \delta\mathbf{R}_R)\,\mathrm{d}\tau_R - \int_\zeta (\overline{\sigma}_k \delta U_k - \overline{\sigma}\delta\psi)\,\mathrm{d}\zeta \right] \mathrm{d}t = 0 \tag{10}$$

where

$$\tilde{\mathcal{H}} = \frac{1}{2}[\sigma_{ss}\varepsilon_{ss} + \sigma_{zz}\varepsilon_{zz} + \tau_{sz}\gamma_{sz} + \tau_{nz}\gamma_{nz} - \mathcal{E}_{31}E_3\varepsilon_{ss} - \mathcal{E}_{32}E_3\varepsilon_{zz} - \xi_{11}E_2^2 - \zeta_{33}E_3^2] \tag{11}$$

$$\mathbf{R} = [x+u]\mathbf{i} + [y+v]\mathbf{j} + [R_0+z+w]\mathbf{k} \tag{12}$$

$$\mathbf{R}_R = u_o\mathbf{i} + v_o\mathbf{j} + (L+w_o+R_0)\mathbf{k} + x\mathbf{i}_R + y\mathbf{j}_R + (r_m+z)\mathbf{k}_R \tag{13}$$

Here τ, τ_R, and ζ denote the beam-volume, rotor-volume, and beam-surface, respectively; $\overline{\sigma}_k$, U_k, $\overline{\sigma}$, ψ, $\tilde{\mathcal{H}}$, $\mathbf{R}$, and $\mathbf{R}_R$ denote surface traction vector, displacement vector, applied surface charge density, electric potential, electric enthalpy, position vector for deformed beam, and position vector for rotor, respectively; ξ_{ij} and ζ_{ij} denote dielectric and reduced dielectric constants, respectively (Appendix A).

A vertical (y-directed) line load, $p_y[z,t]$ is considered. The resulting seven electromechanical equations of motion (EOM) and BC's are in terms of displacement field variables u_o, v_o, θ_x, θ_y, w_o, ϕ, and electric potential ψ_o, which depend on $[z,t]$.

Since the beam is directed radially outward from the hub, Coriolis effects due to beam rotation (Ω) are neglected [32]. The beam is assumed stiffer in the longitudinal direction, (i.e., $(w_o, \ddot{w}_o) \ll (u_o, v_o)$), and the circumferentially uniform stiffness (CUS) ply angle configuration is considered. This yields a linearized and coupled system governing the motion (bending—transverse shear, i.e., flap-lag, and extension-twist) and the electric potential. The coupling occurs via ψ_o. Note that the present model considers the coupled electro-mechanical system, i.e., the electric field $\psi_o(z,t)$ equation is one of the seven coupled governing equations. This was not considered in [18,29]. Therein the electric field variation in thickness and spanwise direction was neglected, i.e., $E_3 = u[t]/t_P$ where $u[t]$ is the amplified control voltage applied to actuators, thus resulting in six equations governing mechanical field variables only. When such a spatially constant electric potential is assumed, flap-lag and extension-twist motions decouple [29,18] in contrast to the present case. The present governing system is obtained as

$$\begin{aligned}\underline{\underline{\delta u_o}}:\quad & \{[\delta_h I_1+\delta_e I_7](\ddot{u}_o'-\Omega^2 u_o')\}'+\{[\delta_h I_5+\delta_e I_9](\ddot{v}_o'-\Omega^2 v_o')\}'+\delta_h\{[I_3-I_1](\ddot{\theta}_y-\Omega^2\theta_y)\}'-\delta_h\{[I_6-I_5](\ddot{\theta}_x-\Omega^2\theta_x)\}'\\ & -b_1(\ddot{u}_o-\Omega^2 u_o)-\delta_e(a_{22}u_o''+a_{23}v_o'')''+(b_1\Omega^2 R u_o')'+\delta_t\{(a_{44}+\delta_h\tilde{a}_1)(u_o'-\theta_y)+(a_{43}+\delta_h\tilde{a}_2)\theta_x'\\ & +(\delta_h\tilde{a}_{30}-a_{42})\theta_y'+(a_{45}+\delta_h\tilde{a}_{31})(\theta_x+v_o')\}'+\delta_h\{[\tilde{a}_3 v_o''+\tilde{a}_{32}u_o'']'+[\tilde{a}_5\theta_y'-\tilde{a}_6 u_o''-\tilde{a}_4(\theta_x+v_o')\\ & -\tilde{a}_{34}\theta_x'-\tilde{a}_{35}v_o''-\tilde{a}_{32}(u_o'-\theta_y)]''\}-\delta_t(m_\beta a_{P4}\psi_o-l_\beta^2 a_{P8}\psi_o')'+\delta_e(l_\beta a_{P8}\psi_o)''+\delta_h(l_\beta a_{P7}\psi_o)''=0\end{aligned}\tag{14}$$

$$\begin{aligned}\underline{\underline{\delta\theta_y}}:\quad & \delta_t[\delta_h(2I_3-I_1)-I_7](\ddot{\theta}_y-\Omega^2\theta_y)-\delta_h(I_3-I_1)(\ddot{u}_o'-\Omega^2 u_o')-\delta_h(I_6-I_5)(\ddot{v}_o'-\Omega^2 v_o')-\delta_t[\delta_h(2I_6-I_5)-I_9](\ddot{\theta}_x-\Omega^2\theta_x)\\ & +\delta_h\{\tilde{a}_3 v_o''+\tilde{a}_{32}u_o''-(\tilde{a}_{34}v_o''+\tilde{a}_5 u_o'')'\}+\delta_t\{(a_{43}+\delta_h\tilde{a}_2)\theta_x'-(a_{44}+\delta_h\tilde{a}_1)(\theta_y-u_o')+(\delta_h\tilde{a}_{30}-a_{42})\theta_y'\\ & +(a_{45}+\delta_h\tilde{a}_{31})(\theta_x+v_o')\}+\delta_t\{(a_{22}+\delta_h\tilde{a}_{11})\theta_y'-(a_{52}+\delta_h\tilde{a}_8)(\theta_x+v_o')-(\delta_h\tilde{a}_{33}+a_{23})\theta_x'-(a_{24}-\delta_h\tilde{a}_{30})(u_o'-\theta_y)\}'\\ & -\delta_t([l_\beta a_{P5}\psi_o]'+[m_\beta a_{P4}\psi_o-l_\beta^2 a_{P8}\psi_o'])=0\end{aligned}\tag{15}$$

$$\begin{aligned}\underline{\underline{\delta v_o}}:\quad & \{[\delta_h I_2+\delta_e I_8](\ddot{v}_o'-\Omega^2 v_o')\}'+\{[\delta_h I_5+\delta_e I_9](\ddot{u}_o'-\Omega^2 u_o')\}'-\delta_h\{[I_4-I_2](\ddot{\theta}_x-\Omega^2\theta_x)\}'+\delta_h\{[I_6-I_5](\ddot{\theta}_y-\Omega^2\theta_y)\}'\\ & -b_1\ddot{v}_o+(b_1\Omega^2 R v_o')'-\delta_e(a_{33}v_o''+a_{23}u_o'')''+\delta_t\{(a_{45}+\delta_h\tilde{a}_{31})(u_o'-\theta_y)+(a_{35}+\delta_h\tilde{a}_{30})\theta_x'-(\delta_h\tilde{a}_8+a_{52})\theta_y'\\ & +(a_{55}+\delta_h\tilde{a}_7)(\theta_x+v_o')\}'+\delta_h\{[-\tilde{a}_{32}v_o''+\tilde{a}_4 u_o'']'+[\tilde{a}_{34}\theta_y'-\tilde{a}_{10}v_o''+\tilde{a}_{32}(\theta_x+v_o')-\tilde{a}_9\theta_x'-\tilde{a}_{35}u_o''-\tilde{a}_3(u_o'-\theta_y)]''\}\\ & +p_y[z,t]-\delta_t(l_\beta a_{P4}\psi_o-l_\beta m_\beta a_{P8}\psi_o')'-\delta_e(m_\beta a_{P8}\psi_o)''+\delta_h(m_\beta a_{P7}\psi_o)''=0\end{aligned}\tag{16}$$

$$\begin{aligned}\underline{\underline{\delta\theta_x}}:\quad & \delta_t[\delta_h(2I_4-I_2)-I_8](\ddot{\theta}_x-\Omega^2\theta_x)+\delta_h(I_4-I_2)(\ddot{v}_o'-\Omega^2 v_o')+\delta_h(I_6-I_5)(\ddot{u}_o'-\Omega^2 u_o')+\delta_t[\delta_h(I_5-2I_6)+I_9](\ddot{\theta}_y-\Omega^2\theta_y)\\ & +\delta_h\{\tilde{a}_{32}v_o''-\tilde{a}_4 u_o''+(\tilde{a}_{34}u_o''+\tilde{a}_9 v_o'')'\}+\delta_t\{(a_{25}+\delta_h\tilde{a}_8)\theta_y'+(a_{45}+\delta_h\tilde{a}_{31})(\theta_y-u_o')-(a_{35}+\delta_h\tilde{a}_{30})\theta_x'\\ & -(a_{55}+\delta_h a_7)(\theta_x+v_o')\}+\delta_t\{(a_{33}+\delta_h\tilde{a}_{12})\theta_x'+(\delta_h\tilde{a}_2+a_{43})(u_o'-\theta_y)-(a_{23}+\delta_h\tilde{a}_{33})\theta_y'+(a_{35}+\delta_h\tilde{a}_{30})(\theta_x+v_o')\}'\\ & -\delta_t([m_\beta a_{P5}\psi_o]'-[l_\beta a_{P4}\psi_o-l_\beta m_\beta a_{P8}\psi_o'])=0\end{aligned}\tag{17}$$

$$\underline{\underline{\delta w_o}}:\quad (a_{11}^p w_0')'+(\tilde{a}_{17}^p\phi')'-b_1\{\ddot{w}_o-\Omega^2(R_0+z+w_o)\}-(a_{P1}\psi_o)'=0\tag{18}$$

$$\begin{aligned}\underline{\underline{\delta\phi}}:\quad & (I_{\omega\omega}^p\ddot{\phi}')'-(I_{xx}^p+I_{yy}^p)\ddot{\phi}+(b_1\Omega^2\hat{I}_P R\phi')'+\Omega^2[(I_{xx}^p-I_{yy}^p)(m_\beta^2-l_\beta^2)\phi-(I_{\omega\omega}^p\phi')']+\Omega^2(I_{yy}^p-I_{xx}^p)m_\beta l_\beta+(\tilde{a}_{17}^p w_o')'+(\tilde{a}_{77}^p\phi')'\\ & -(a_{66}^p\phi'')''-(a_{P6}\psi_o)'=0\end{aligned}\tag{19}$$

$$\begin{aligned}\underline{\underline{\delta\psi_o}}:\quad & L_{P22}\psi_o''+a_{P1}w_o'+m_\beta a_{P5}\theta_x'+l_\beta a_{P5}\theta_y'-m_\beta(a_{P8}-a_{P7})v_o''+l_\beta(a_{P8}-a_{P7})u_o''+a_{P6}\phi'-m_\beta a_{P4}u_o'-l_\beta a_{P4}v_o'\\ & +m_\beta a_{P5}\theta_x+m_\beta a_{P4}\theta_y-L_{P33}\psi_o=a_{P10}\overline{\sigma}\end{aligned}\tag{20}$$

Here ($\tilde{a}_{ij}[z]$, $a_{ij}[z]$) are global stiffnesses, the former including pretwist and HSDT effects; $(I_1,\ldots,I_9,I_{xx}^p,I_{yy}^p,I_{\omega\omega}^p,b_1,\hat{I}_P)$ are structural inertia and mass quantities; a_{Pi} are global piezoelectric coefficients; and $R[z]=R_0(L-z)+0.5(L^2-z^2)+m_R(R_0+L+r_m)/b_1$ contains the centrifugal stiffening effect (see Appendix A and [18]). The BC's at the clamped end (z=0) are $u_o=v_o=\theta_y=\theta_x=u_o'=v_o'=w_o=\phi=\phi'=\psi_o=0$.

2.5. Discretization

The extended Galerkin method (EGM) [33,34,4,7] is used since the natural BC's at the beam tip are complicated. This method employs admissible trial functions, i.e., those that need only satisfy geometric BC's. For governing systems derived from a variational principle, like herein, the method is as follows. The residual—using the approximate solution—is formed by weighting EOM's (Eqs. (14)–(20)) and natural BC's with their respective variation (e.g., $\delta\theta_x$ for Eq. (17)), and adding individual residuals. Galerkin integrals are then evaluated to yield system matrices that contain contributions from natural boundary terms also (since residual includes non-satisfaction of natural BC's). Alternatively, the quadratic energy functional (like in Eq. (10)) is obtained by suitable integrations in the above residual with beam Coriolis forces neglected. The approximate solution is then substituted and functional (equivalent to residual) is minimized via Hamilton's principle, i.e., the variational process minimizes error in not satisfying natural BC's and EOM to yield the discretized system (see Appendix B). The approximate solution is considered of the form,

$$\{u_o,v_o,w_o,\theta_x,\theta_y,\phi,\psi_o\}=\{\mathbf{\Phi}_1^{\mathrm{T}}[z]\mathbf{q}_1[t],\ldots,\mathbf{\Phi}_7^{\mathrm{T}}[z]\mathbf{q}_7[t]\}\tag{21}$$

where $\boldsymbol{\Phi}_\mathbf{i}$ and $\mathbf{q}_\mathbf{i}$ $(i=1,\ldots,7)$ are N-dimensional column vectors of trial functions and generalized coordinates, respectively. The surface charge density due to voltage applied on actuators is given by

$$\overline{\sigma}[z,t]=\boldsymbol{\Phi}_\mathbf{7}^{\mathrm{T}}[z]\hat{\boldsymbol{\sigma}}[t] \tag{22}$$

where $\hat{\boldsymbol{\sigma}}|_{N\times 1}$ is the time dependent charge density vector applied on actuators, i.e., the control input to be determined via LQR control. Using this to eliminate (i.e., statically condense) the electrical degree of freedom ψ_o via Eq. (20), the discretized system

$$\mathbf{M}\ddot{\mathbf{q}}+\mathbf{G}\dot{\mathbf{q}}+\mathbf{K}\mathbf{q}=\mathbf{Q}[t]-\mathbf{F}\hat{\sigma}[t],\quad \mathbf{q}=\left\{\mathbf{q}_\mathbf{1}^{\mathrm{T}}|\cdots|\mathbf{q}_\mathbf{6}^{\mathrm{T}}\right\}^{\mathrm{T}} \tag{23}$$

results from the displacement governing Eqs. (14)–(19). Here $\mathbf{G}|_{6N\times 6N}$, $\mathbf{Q}|_{6N\times 1}$, and $\mathbf{F}|_{6N\times N}$ represent the gyroscopic matrix due to rotor (arising from force BC's at the free end), external forcing, and piezoelectrically induced forcing coefficients, respectively, while $\mathbf{M}|_{6N\times 6N}$ and $\mathbf{K}|_{6N\times 6N}$ are the mass and stiffness matrices, respectively (see Appendix B and [18]).

3. Optimal control

3.1. Sensor output

Applying Gauss' law on the exposed surface of sensors, the total charge generated on the i th sensor due to the direct effect is

$$\tilde{q}_{Pi}=\int_{z_i^-}^{z_i^+}\oint_s D_3\mathcal{S}_s f_z\,\mathrm{d}s\,\mathrm{d}z\bigg|_{n=h/2} \tag{24}$$

Since no voltage is applied to sensors and strain $\varepsilon_{ss}=0$, the n-component of electric displacement is $D_3=\mathcal{E}_{31}\varepsilon_{zz}$. Introducing the strain $\varepsilon_{zz}(=w')$ as obtained from Eq. (5), and performing the spatial discretization yields $\tilde{q}_{Pi}[t]=\mathbf{C}_i\mathbf{q}$. Here $\mathbf{C}_i=[\mathbf{C}_{i1}|\cdots|\mathbf{C}_{i6}]$, with $\mathbf{C}_{ij}$, $j=1,\ldots,6$, being N-dimensional row vectors [18]. The sensor patches are treated as capacitors with capacitance $C_P=\xi_{33}A_P/t_P$, where A_P is the patch surface area. Since the energy stored in a piezoelectric transducer consists of mechanical and electrical components, the capacitance depends on relative stiffness between transducer and host; i.e., it varies between the blocked value (corresponding to constant deformation) and the free value (corresponding to constant stress) [35]. However, following [4], in the present case the free deformation capacitance is considered. The charge applied on actuators is due to the amplified output of the sensors. It is obtained from the applied charge density $\overline{\sigma}$ by integration over the surface. Hence, using Eq. (22), the voltage applied on the i th actuator is

$$u_i[t]=1/C_P\int_{z_i^-}^{z_i^+}\int_0^{2\kappa}\boldsymbol{\Phi}_\mathbf{7}^{\mathrm{T}}\hat{\sigma}[t]\mathcal{A}_s f_z\,\mathrm{d}s\,\mathrm{d}z \tag{25}$$

In the present case a single sensor–actuator pair extending over the length of the beam is considered, i.e., $z_i^-=0$ and $z_i^+=L$, with a single control voltage u replacing the u_i. The current from sensors is $I[t]=\dot{\tilde{q}}_P$ and power required is $P[t]=u[t]I[t]$

3.2. LQR control

Using $\mathbf{x}=\{\mathbf{q}^{\mathrm{T}}|\dot{\mathbf{q}}^{\mathrm{T}}\}^{\mathrm{T}}$, the state space representation of the system is

$$\dot{\mathbf{x}}=\mathbf{A}\mathbf{x}+\mathbf{B}\hat{\boldsymbol{\sigma}}+\mathbf{W}\mathbf{Q},\quad \mathbf{A}=\begin{bmatrix}\mathbf{0} & \mathbf{I}\\ -\mathbf{M}^{-1}\mathbf{K} & \mathbf{0}\end{bmatrix},\quad \mathbf{W}=\begin{bmatrix}\mathbf{0}\\ \mathbf{M}^{-1}\end{bmatrix},\quad \mathbf{B}=\begin{bmatrix}\mathbf{0}\\ -\mathbf{M}^{-1}\mathbf{F}\end{bmatrix} \tag{26}$$

One seeks the control input vector $\hat{\boldsymbol{\sigma}}[t]$ (i.e., time dependent charge density vector) that minimizes the cost index

$$J=\int_0^\infty \frac{1}{2}\left(\mathbf{x}^{\mathrm{T}}\mathbf{Z}\mathbf{x}+\hat{\boldsymbol{\sigma}}^{\mathrm{T}}\mathbf{R}\hat{\boldsymbol{\sigma}}\right)\mathrm{d}t \tag{27}$$

The above multi-input LQR problem is cast in terms of charge density vector $\hat{\boldsymbol{\sigma}}[t]$ as the control input. Actuator voltages are then obtained from Eq. (25) for collocated sensor–actuator pairs. Here $\mathbf{Z}$ is the positive semidefinite state weighting matrix representing mechanical energy and thus satisfying $\mathbf{Z}\mathbf{x}=\left[\alpha\mathbf{q}^{\mathrm{T}}\mathbf{K}^{\mathrm{T}}|\mu\dot{\mathbf{q}}^{\mathrm{T}}\mathbf{M}^{\mathrm{T}}\right]^{\mathrm{T}}$, and $\mathbf{R}$ is the positive definite control weighting matrix chosen as $\mathbf{R}=\eta\mathbf{F}^{\mathrm{T}}\mathbf{K}^{-1}\mathbf{F}$, and α,μ,η are suitably chosen weights. The cost minimization, i.e., $\delta J=0$, yields the optimal control input

$$\hat{\boldsymbol{\sigma}}=-\tilde{\mathbf{G}}\mathbf{x},\quad \tilde{\mathbf{G}}=\mathbf{R}^{-1}\mathbf{B}^{\mathrm{T}}\mathbf{P} \tag{28}$$

where $\mathbf{P}$ is the solution of the algebraic Riccati equation (ARE)

$$\mathbf{A}^{\mathrm{T}}\mathbf{P}+\mathbf{P}\mathbf{A}-\mathbf{P}\mathbf{B}\mathbf{R}^{-1}\mathbf{B}^{\mathrm{T}}\mathbf{P}+\mathbf{Z}=\mathbf{0} \tag{29}$$

The ARE is solved using the stable eigenvectors of the Hamiltonian matrix of the LQR system [36]. Hence, using Eq. (25) the i th actuator voltage for optimal control is obtained as

$$u_i[t] = -\hat{\mathbf{G}}_i \mathbf{x} \quad \text{where } \hat{\mathbf{G}}_i = 1/C_P \int_{z_i^-}^{z_i^+} \int_0^{2\kappa} \mathbf{\Phi}_7^{\mathrm{T}} \mathbf{R}^{-1} \mathbf{B}^{\mathrm{T}} \mathbf{P} \mathcal{A}_s f_z \, \mathrm{d}s \, \mathrm{d}z \tag{30}$$

Thus, the ratio between actuator input voltage and sensor output voltage for the i th piezo-pair is $-C_P \hat{\mathbf{G}}_i \mathbf{x} / [\mathbf{C}_i | \mathbf{0}] \mathbf{x}$. In order to avoid saturation of the piezoactuators the voltage is limited to $\mathrm{sgn}[u_i] V_{\max}$ whenever $|u_i| \geq V_{\max}$, where $V_{\max}$ is the actuator saturation voltage.

4. Results and discussions

A single ply Graphite-Epoxy host structure is considered. Its properties [29] are given in Table 1, for which subscripts 1 and 2, 3 denote directions parallel and transverse to the fiber, respectively. Table 1 also lists properties [29] of the identical PZT-4 piezopatches considered, for which subscripts 1, 2, and 3 denote directions parallel to the pretwisted beam axis, parallel to the x^p axis, and parallel to the y^p axis, respectively. The geometric data used are also given in Table 1. The weights $\alpha = 1$, $\mu = 1$, and $\eta = 10$ are used so as to compare results with [18]. The values $\alpha = 1$ and $\mu = 1$ imply that the first term in cost index, J, equals the total mechanical energy of the system. The choice $\eta = 10$ yields reasonable attenuation. A study of the choice of weights represents a separate optimization problem by itself and is not considered herein. A method to choose **Z** (state weighting) by using the controllability grammian and **B** (control input matrix) is given in Gawronski [37]. This procedure ensures that each state is penalized, in the cost index, in inverse proportion to its degree of controllability. Though not adopted here, this procedure is expected to yield efficient control once η is optimized.

Results are obtained for a single continuous pair of piezopatches. The trial functions chosen are polynomial series satisfying BC's at the root. They are

$$\mathbf{\Phi_1} = \mathbf{\Phi_2} = \mathbf{\Phi_6} = \left\{ z^2 \;\; z^3 \;\; z^4 \ldots \right\}^{\mathrm{T}}, \quad \mathbf{\Phi_3} = \mathbf{\Phi_4} = \mathbf{\Phi_5} = \mathbf{\Phi_7} = \left\{ z \;\; z^2 \;\; z^3 \ldots \right\}^{\mathrm{T}} \tag{31}$$

In this regard it should be noted that modal analysis for beams with distributed piezopatches was studied by Maurini et al. [38]. In order to model curvature discontinuities in mode shapes, arising due to discontinuous piezopatches, they proposed an enhanced assumed modes method with jump functions included in the basis functions. Results for natural frequencies were shown to compare well with standard assumed modes method, 1D FEM, and exact eigenvalue problem solved by least error norm method. However, mode shapes compared well only with the exact method. Their proposed method would be useful in control applications with distributed piezo elements. Maxwell and Asokanathan [39] used a segmentation procedure to model nonuniform beams with distributed actuators. Therein Timoshenko beam segments with uniform properties are interconnected, and the mode shapes obtained for each segment are placed end-to-end to yield the overall mode shape. However, using the present formulation, results can also be obtained for distributed pairs of patches by using the trial functions in Eq. (31), as done in [40], and these results can be compared with the ones obtained from either of the methods in [38,39]. This, however, is beyond the scope of the present work.

A uniformly distributed excitation is considered, i.e., $p_y[z,t]=p_y[t]$, with initial magnitude $p_m \equiv p_y[0]$. The response due to step loading, triangular pulse, and sonic boom loading is presented. Unless mentioned otherwise, the results pertain to the HSDT and are obtained for a linearly pretwisted beam, with $\Omega = 100\,\mathrm{rad\,s^{-1}}$, $p_m = 875.63\,\mathrm{N\,m^{-1}}$. As mentioned in Section 3.1, in the present numerical study the piezopatch pair is taken to extend over the span, resulting in a single control voltage being obtained for application to the single actuator. For the controlled case, the nondimensional tip response $v^*[t]=v_o[L,t]/L$, control voltage $u[t]$ and power $P[t]$ are plotted. These correspond to the fully coupled (flap-lag-extension-twist) motion.

Figs. 3–5 relate to modal convergence studies. In Figs. 3 and 4, the first and second flap bending modes are shown for ply angle $\theta = 0^\circ$ and beam angular speeds $\Omega = 0$, 500 rad/s, using a N=2, 4, 6, 8 term series of trial functions. Fig. 3 shows that for the first mode, as the beam speed increases the differences increase between the N=2 result compared to the N=4,

Table 1
Material and geometric properties of system.

Material properties of orthotropic host		
$E_1^H = 20.68 \times 10^{10}\,\mathrm{N\,m^{-2}}$	$E_2^H = 5.17 \times 10^{9}\,\mathrm{N\,m^{-2}}$	$G_{12}^H = G_{13}^H = 2.55 \times 10^{9}\,\mathrm{N\,m^{-2}}$
$G_{23}^H = 3.1 \times 10^{9}\,\mathrm{N\,m^{-2}}$	$\nu_{12}^H = \nu_{13}^H = \nu_{23}^H = 0.25$	$\rho^H = 1,528.15\,\mathrm{kg\,m^{-3}}$
Material properties of PZT-4 piezopatch		
$C_{11}^P = 1.3897 \times 10^{11}\,\mathrm{N\,m^{-2}}$	$C_{12}^P = 7.7757 \times 10^{10}\,\mathrm{N\,m^{-2}}$	$C_{13}^P = 7.4283 \times 10^{10}\,\mathrm{N\,m^{-2}}$
$C_{33}^P = 1.1497 \times 10^{11}\,\mathrm{N\,m^{-2}}$	$C_{44}^P = 2.5593 \times 10^{10}\,\mathrm{N\,m^{-2}}$	$\rho^P = 7,494.88\,\mathrm{kg\,m^{-3}}$
$e_{31} = -5.2\,\mathrm{N\,m^{-1}\,V^{-1}}$	$e_{33} = 15.098\,\mathrm{N\,m^{-1}\,V^{-1}}$	$\xi_{33} = 4.009 \times 10^{-6}\,\mathrm{C^2\,N^{-1}\,m^{-2}}$
Geometric properties of hub, beam, piezopatch, and rotor		
$R_0 = 0.2032\,\mathrm{m}$	$L = 2.032\,\mathrm{m}$	$b_{tip} = 0.0254\,\mathrm{m}$; $c_{tip} = 0.127\,\mathrm{m}$
$h = 0.0127\,\mathrm{m}$	$\sigma = 0.25$	$\kappa = 0.0381\,\mathrm{m}$
$t_P = 0.00127\,\mathrm{m}$	$m_R = 1\,\mathrm{kg}$	$r_m = k_R = 0.2\,\mathrm{L}$

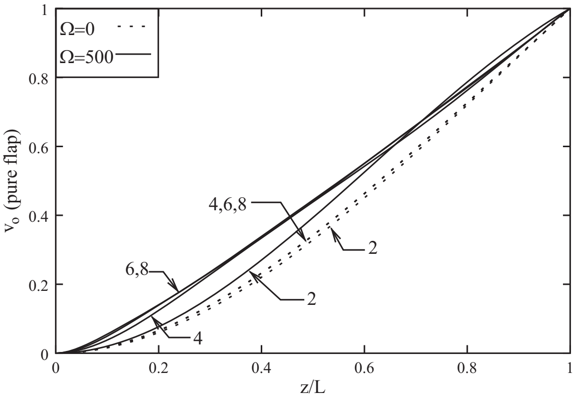

Fig. 3. First pure flap mode using 2, 4, 6, 8 term expansion (ply-angle $\theta = 0^\circ$).

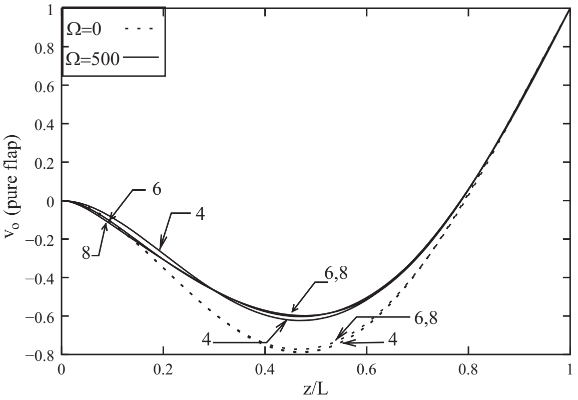

Fig. 4. Second pure flap mode using 4, 6, 8 term expansion (ply-angle $\theta = 0^\circ$).

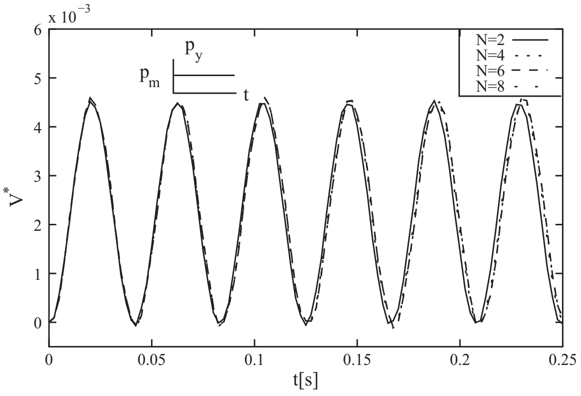

Fig. 5. Uncontrolled tip response using 2, 4, 6, 8 term expansion (ply-angle $\theta = 60^\circ$, beam speed $\Omega = 100\,\text{rad/s}$).

6, 8 results. For both modes, the results using N = 4, 6, 8 are close to each other even for $\Omega = 500\,\text{rad/s}$, although there do exist marginal differences when considering N=4. The uncontrolled response, $v_*[t]$, for step excitation, $\theta = 60^\circ$ and $\Omega = 100\,\text{rad/s}$, is shown in Fig. 5 for $N = 2, \ldots, 8$. The response appears to have converged for $N \geq 4$, for which the period increases, thus indicating a decrease in fundamental frequency as the number of trial functions is increased (i.e., as expected the eigenfrequencies converge from above). Based on modal convergence obtained during eigenvibration and uncontrolled response studies, the number of trial functions was chosen as N=4.

Table 2 shows the first two eigenfrequencies in flap bending as the nondimensional beam angular speed $\hat{\Omega}(\equiv \Omega(b_1 L^4/a_{33}))$ and nondimensional tip rotor mass $m_t(\equiv \Omega(m_R/b_1 L))$ are varied. Results from [41] using FEM and from [42] using the Frobenius method are compared with those from the present theory, by specializing the latter for an unshearable, untwisted, untapered beam, with zero rotor speed, zero rotor mass moment of inertia (i.e., rotor reduced to a point mass), and zero hub radius. The comparison appears very good, with maximum error being 0.34 and 2.82 percent for $\overline{\varpi}_1$ and $\overline{\varpi}_2$, respectively, occurring for $\hat{\Omega}=6$. As the tip mass is increased, for the range of beam speeds considered the fundamental flapping frequency shows a consistent softening behavior. However, a reversal from softening to hardening

Table 2

Comparison with [41,42], first and second flapping frequencies, $\overline{\varpi}_1$ and $\overline{\varpi}_2$, for selected values of beam angular speed $\hat{\Omega}$ and tip mass ratio m_t.

m_t	$\hat{\Omega}$	$\overline{\varpi}_1$			$\overline{\varpi}_2$		
		[41]	[42]	Present	[41]	[42]	Present
0	0	3.5160	3.5160	3.5020	22.0352	22.0345	21.4427
1	0	1.5573	1.5573	1.5560	16.2504	16.2500	16.0636
0	3	4.7973	4.7973	4.7794	23.3210	23.3203	22.6901
1	3	3.5823	3.5823	3.5797	20.3507	20.3504	20.1192
0	6	7.3604	7.3604	7.3354	26.8098	26.8091	26.0744
1	6	6.5092	6.5090	6.5047	29.2926	29.2917	28.9665
0	9	10.2258	10.2257	10.1936	31.7716	31.7705	30.8854
1	9	9.4904	9.4899	9.4838	39.8082	39.8048	39.3719
0	12	13.1706	13.1702	13.1311	37.6050	37.6031	36.5378
1	12	12.4827	12.4814	12.4735	50.8684	50.8594	50.3150

Table 3

Comparison with [43], first and second flapping frequencies, $\overline{\varpi}_1$ and $\overline{\varpi}_2$, for selected values of tip mass ratio m_t.

m_t	$\hat{\Omega}=1$				$\hat{\Omega}=100$			
	$\overline{\varpi}_1$		$\overline{\varpi}_2$		$\overline{\varpi}_1$		$\overline{\varpi}_2$	
	[43]	Present	[43]	Present	[43]	Present	[43]	Present
0.0	3.6816	3.6787	22.181	22.0611	101.31	101.2301	248.67	247.8445
0.02	3.5548	3.5522	21.405	21.2951	101.27	101.1965	249.24	248.5050
0.04	3.4414	3.4389	20.789	20.6869	101.23	101.1664	250.83	250.1720
0.5	2.2930	2.2920	17.227	17.1609	100.90	100.8698	322.58	322.1873
1	1.9017	1.9010	16.757	16.6962	100.80	100.7782	392.32	391.9386
2	1.5902	1.5897	16.725	16.6669	100.72	100.7122	504.66	504.2376
5	1.3222	1.3219	17.490	17.4339	100.67	100.6622	746.95	746.4019
10	1.2052	1.2049	18.972	18.9172	100.65	100.6433	1031.40	1030.6337

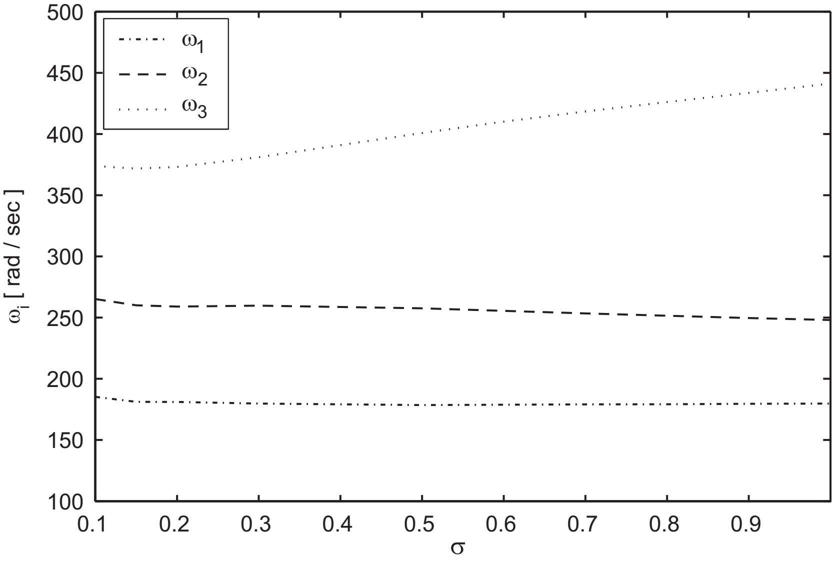

Fig. 6. Effect of taper σ on eigenfrequencies ω_i (rotor mass m_R=1 kg, linear pretwist $\beta_0=15^\circ$, ply-angle $\theta=45^\circ$, beam speed $\Omega=200$ rad/s, rotor speed $\overline{\Omega}=200$ rad/s).

behavior occurs for the second flap frequency for $\hat{\Omega} \geq 6$. This reversal is due to the tip rotor mass having a softening effect by virtue of added mass, as well as a stiffening effect due to centrifugal forces caused by beam rotation. The latter, i.e., centrifugal stiffening, increases with beam angular speed, and above a certain speed it overcomes the softening effect due to added mass. In Table 3, these eigenfrequencies are compared with results from [43] for $\hat{\Omega} = 1, 100$ and various m_t values. The comparison appears very good, with maximum error being 0.934 percent for $\overline{\varpi}_2$ which occurs for $\hat{\Omega} = 100$ and m_t=0. Here too $\overline{\varpi}_1$ shows consistent softening as m_t is increased at both the angular speeds, while $\overline{\varpi}_2$ stiffens for $m_t \geq 5$ when $\hat{\Omega} = 1$ and stiffens for all m_t when $\hat{\Omega} = 100$, i.e., a reversal from softening to hardening behavior occurs as described above.

The effect of taper on the coupled flap-lag eigenfrequencies is shown in Fig. 6 for pretwist $\beta_0 = 15^\circ$, ply-angle $\theta = 45^\circ$, beam speed $\Omega = 200$ rad/s, and rotor speed $\overline{\Omega} = 200$ rad/s. This shows that a reduction in taper (i.e., increase in taper ratio) has a negligible effect on the first eigenfrequency, a marginal softening effect on the second eigenfrequency, and for $\sigma \geq 0.15$ a distinct stiffening effect on the third eigenfrequency. Thus, increasing taper marginally increases the operation bandwidth (i.e., range of excitation frequencies for non-resonant response) for low frequency input, and decreases the

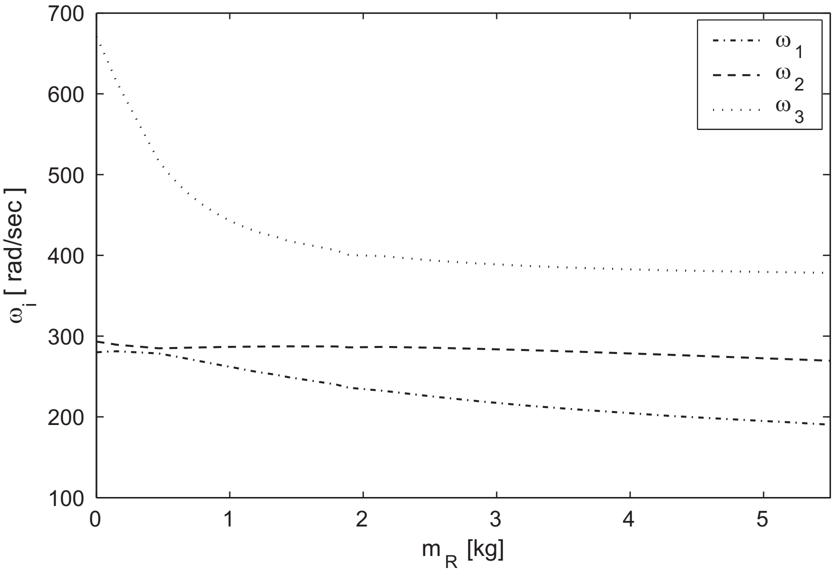

Fig. 7. Effect of tip rotor mass m_R on eigenfrequencies ω_i (taper ratio $\sigma = 0.25$, linear pretwist $\beta_0 = 15^\circ$, ply-angle $\theta = 45^\circ$, beam speed $\Omega = 200$ rad/s, rotor speed $\overline{\Omega} = 200$ rad/s).

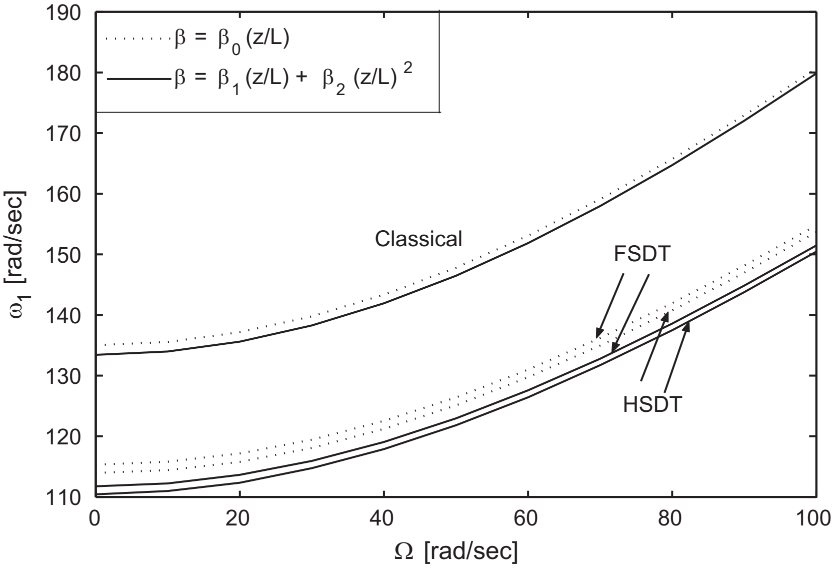

Fig. 8. Effect of beam speed Ω on first eigenfrequency ω_2, three theories compared (rotor mass m_R=1 kg, taper ratio $\sigma = 0.25$, ply-angle $\theta = 90^\circ$, linear and quadratic pretwist $\beta_0 = 90^\circ$, $\beta_1 = \beta_2 = 45^\circ$, rotor speed $\overline{\Omega} = 250$ rad/s).

bandwidth for high frequency input. This trend compares quite well with the results in [6] wherein a solid beam is considered and the inverse of the present definition is used for the taper ratio.

For the same data, Fig. 7 shows the eigenfrequencies as the tip rotor mass is increased. A distinct reduction in the first and third eigenfrequencies is noted for lower values of m_R, thus indicating overall softening behavior for this range of tip rotor mass, i.e., gyroscopic and mass softening dominate over centrifugal stiffening. The second eigenfrequency reduces only marginally when m_R is increased, i.e., gyroscopic and mass softening barely dominate over centrifugal stiffening for this mode. This is due to the fact that the first and third eigenfrequencies correspond to coupled modes in which flap motion is dominant, while the second eigenfrequency is for lag dominated coupled motion. Thus, the second eigenfrequency is only marginally affected by variation in tip rotor mass.

The three formulations, i.e., unshearable, first-order and higher-order shearable theories are compared in Figs. 8–10 for the first three eigenfrequencies. Here linear and quadratically varying pretwist is considered with $\theta = 90^\circ$; $\beta_1 = 45^\circ$; $\beta_2 = 45^\circ$; $\beta_0 = 90^\circ$; $\overline{\Omega} = 250\,\text{rad/s}$. The HSDT formulation yields the lowest coupled natural frequencies, thus providing conservative data for use in attaining non-resonant passive as well as active control designs. This emphasizes the

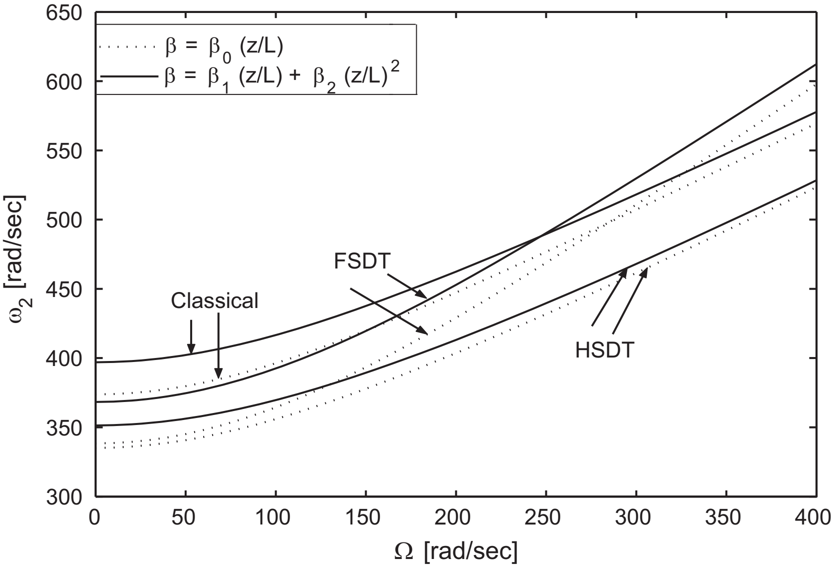

Fig. 9. Effect of beam speed Ω on second eigenfrequency ω_2, three theories compared (data as in Fig. 8).

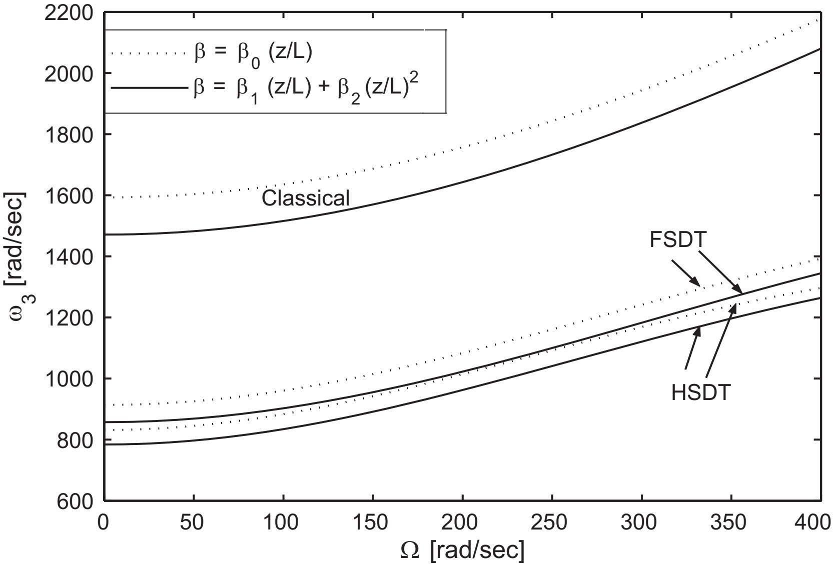

Fig. 10. Effect of beam speed Ω on third eigenfrequency ω_2, three theories compared (data as in Fig. 8).

importance of considering variations in transverse shear across the beam wall. For all three formulations the effect of pretwist distribution (i.e., whether linear or quadratic) diminishes (especially for the second eigenfrequency) as the hub speed increases, for the range of speed considered herein. This is due to predominance of centrifugal stiffening over pretwist effect, at large hub speeds. While the first and third eigenfrequencies are higher for linearly distributed pretwist, the second eigenfrequency is higher for quadratic pretwist. This is due to the second coupled mode being lag dominant as compared to the first and third modes where flap motion dominates. As the hub speed increases, a crossover in the second eigenfrequency predicted by the unshearable and first-order shearable theories is evident for both cases of pretwist. This crossover is due to the presence of the tip rotor which has a greater contribution towards centrifugal stiffening within the first-order formulation.

Figs. 11–14 provide a comparison of the present control scheme where electric field variation along span is considered in the plant model, with the one considered in [18] for a uniform electric field. This pertains to a rotorless untapered beam with step excitation and $\beta_0 = 30^\circ$, $\Omega = 200\,\text{rad/s}$, $\theta = 30^\circ, 60^\circ$. Both plant models predict greater attenuation when the larger ply angle is used (Figs. 11 and 13). This is expected since the bending rigidities increase as the fibers are aligned along the longitudinal, i.e., z, axis of the beam. Note that ply angle is measured with respect to the cross-sectional s-axis, as

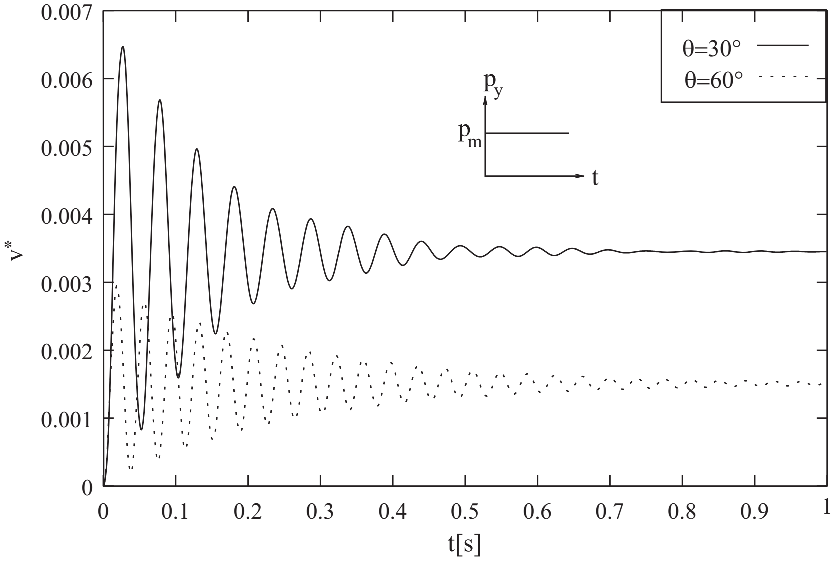

Fig. 11. Effect of ply angle θ on response v^*, untapered, rotorless, step input, uniform electric field assumption [18] (linear pretwist $\beta_0 = 30^\circ$, beam speed $\Omega = 100\,\text{rad/s}$).

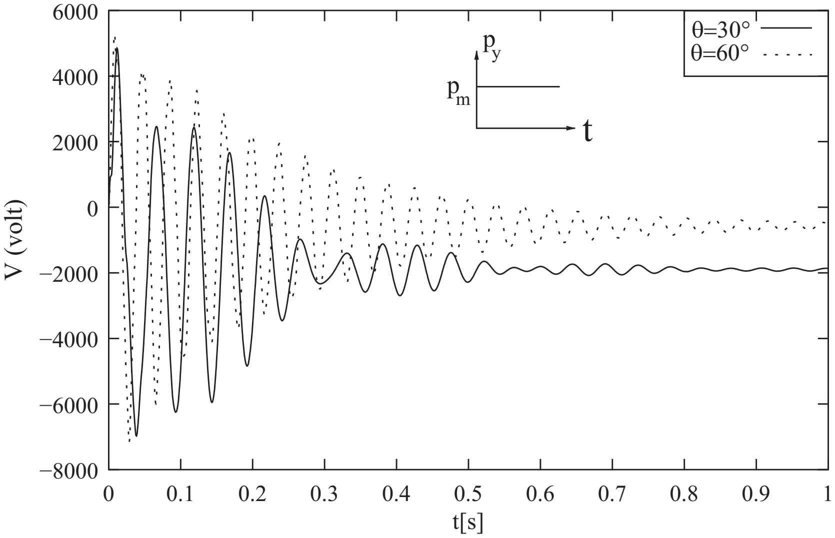

Fig. 12. Effect of ply angle θ on control voltage V, untapered, rotorless, step input, uniform electric field assumption [18] (data as in Fig. 11).

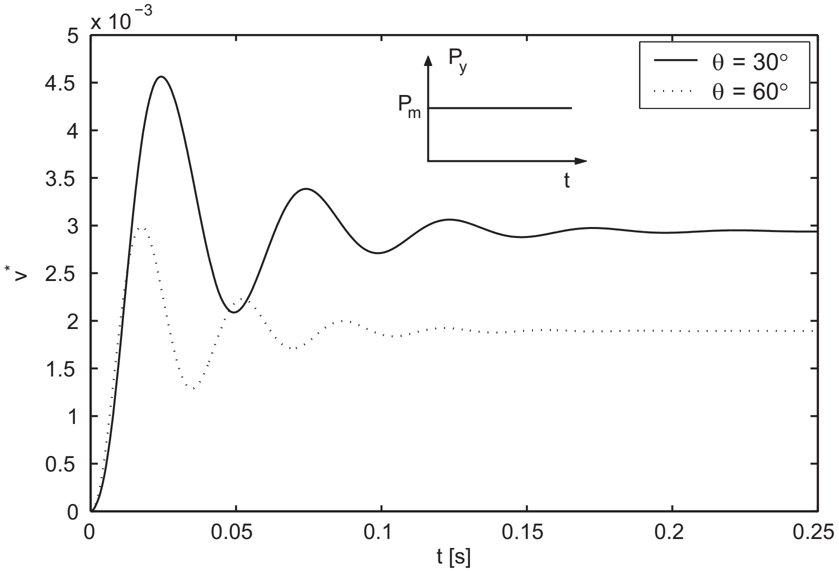

Fig. 13. Effect of ply angle θ on response v^*, untapered, rotorless, step input, nonuniform electric field (present) (data as in Fig. 11).

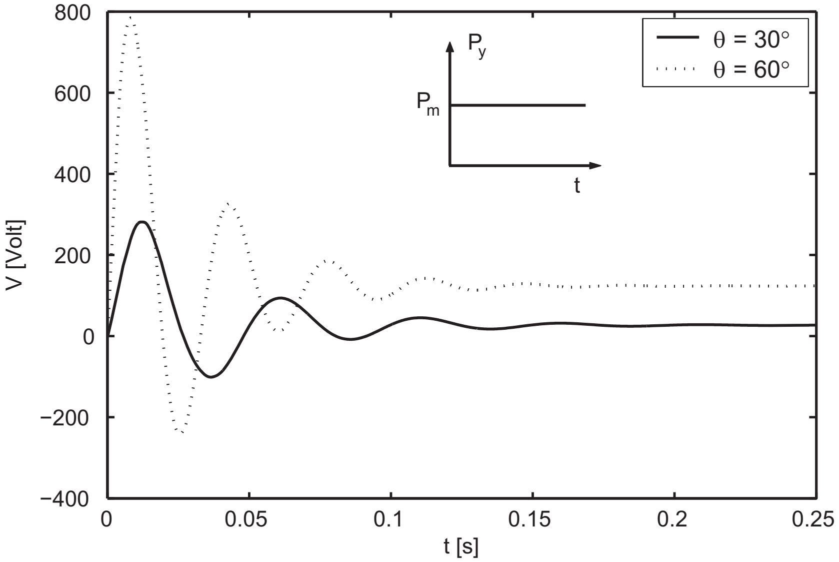

Fig. 14. Effect of ply angle θ on control voltage V, untapered, rotorless, step input, nonuniform electric field (present) (data as in Fig. 11).

is natural for filament wound composites. However, as seen from Fig. 11, a greater rate of attenuation is obtained with smaller ply angle when using plant dynamics with uniform electric field assumption [18]. In contrast, a greater control voltage is required when using the larger ply angle (Figs. 12 and 14), since the more rigid beam requires greater actuation voltage. When comparing Figs. 13 and 14 with Figs. 11 and 12 (reproduced from [18]), it is evident that the present plant model yields an order-of-magnitude reduction in control voltage required. The settling time reduces fivefold, and a 30 percent attenuation in peak response—hence greater overall response attenuation—occurs. This corroborates the result reported in [20] that the electromechanical coupling provides an overall stiffening as compared to the uncoupled system. Since the present plant dynamics represents the actual coupled electromechanical system in contrast to the approximation of decoupling implied in [18], this result shows that the control achievable by LQR design is even better than what was previously reported in [18].

Fig. 15 shows the controlled response for a triangular pulse excitation, when a saturation voltage constraint of 200 V is applied on the actuator voltage. The data used are $\theta = 75^\circ$, $\beta_0 = 30^\circ$, $\Omega = 200$, $\overline{\Omega} = 10\,\text{rad/s}$. The attenuation rate is greatly reduced when using the voltage constraint (as compared to applying an unconstrained voltage assuming no actuator

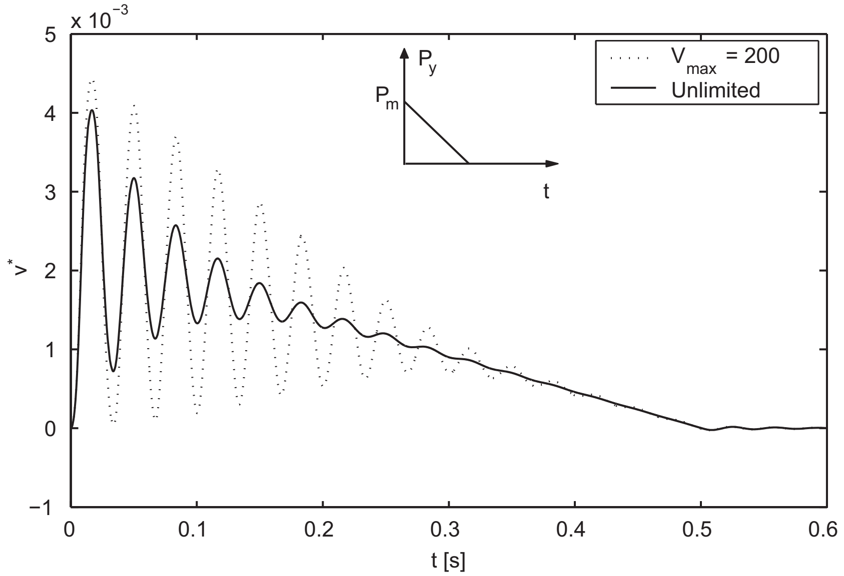

Fig. 15. Effect of voltage constraint on response v^*, triangular pulse input (rotor mass m_R=1 kg, taper ratio $\sigma = 0.25$, ply-angle $\theta = 75^\circ$, linear pretwist $\beta_0 = 30^\circ$, beam speed $\Omega = 100\,\text{rad/s}$ rotor speed $\overline{\Omega} = 10\,\text{rad/s}$).

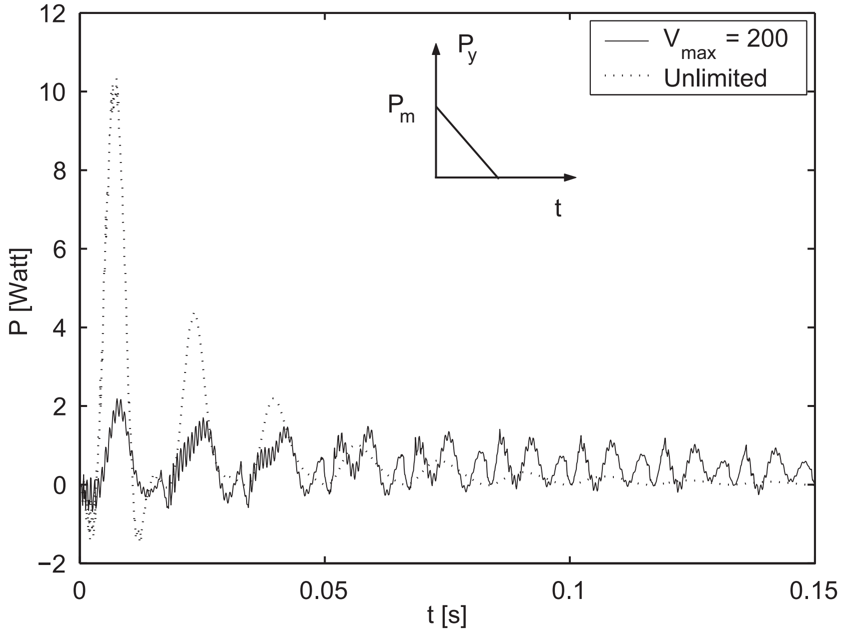

Fig. 16. Effect of voltage constraint on power required P, triangular pulse input (data as in Fig. 15).

saturation) and appears almost linear. The peak tip response for unlimited actuator voltage is around 90 percent of the peak response when using constrained voltage, and corresponding settling times are 0.29 and 0.43 s, i.e., a one-third reduction in settling time for the unconstrained case. However, Fig. 16 shows that the peak power requirement is reduced fivefold when the voltage is constrained. The appearance of higher harmonics in the power requirement is clearly visible when actuator saturation is considered. This is due to frequent clipping of voltage as the saturation limit of 200 V is reached. Thus, despite actuator saturation the control remains quite effective as compared to without actuator saturation, and it also provides tremendous power saving.

When considering structural tailoring along with active control, the rotorless system shows greater response attenuation for a larger ply-angle layup, due to increased bending rigidity, as seen in Fig. 13. In contrast, the system with

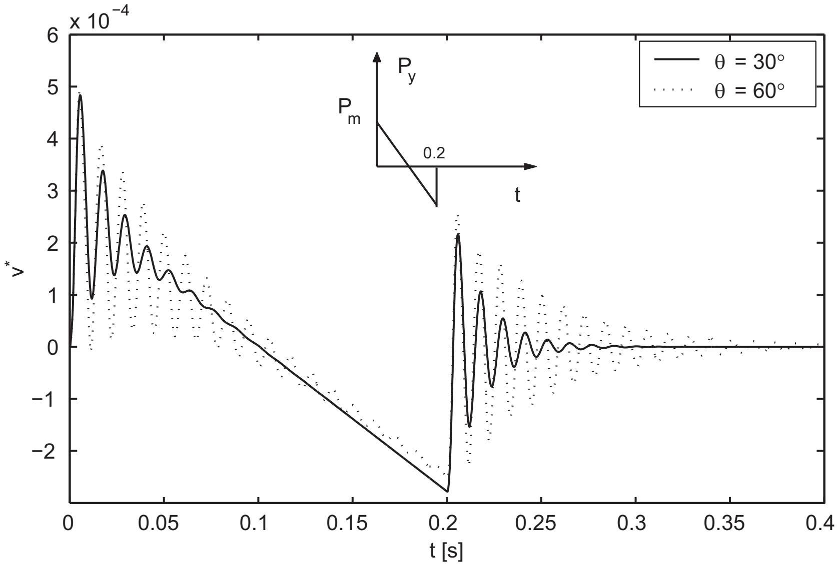

Fig. 17. Effect of ply angle θ on response v^*, sonic boom input (rotor mass m_R=1 kg, taper ratio $\sigma=1$, linear pretwist $\beta_0=30^\circ$, beam speed $\Omega=400\,\mathrm{rad/s}$ rotor speed $\overline{\Omega}=40\,\mathrm{rad/s}$).

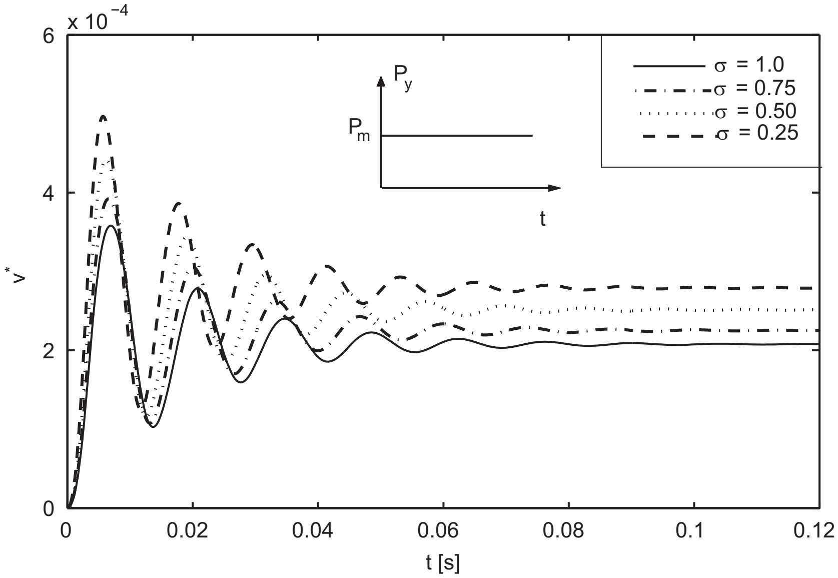

Fig. 18. Effect of taper ratio σ on response v^*, step input (rotor mass m_R=1 kg, ply angle $\theta=30^\circ$, linear pretwist $\beta_0=30^\circ$, beam speed $\Omega=400\,\mathrm{rad/s}$ rotor speed $\overline{\Omega}=40\,\mathrm{rad/s}$).

rotor with m_R=1 kg, $\beta_0=30^\circ$; $\Omega=400\,\mathrm{rad/s}$; $\overline{\Omega}=40\,\mathrm{rad/s}$, and subject to sonic boom excitation, shows a reversal in this trend as seen in Fig. 17. Although peak responses for the two ply angles differ marginally, the attenuation rate for smaller ply angle is distinctly greater, resulting in a settling time of 0.28 s compared to 0.38 s for the larger ply angle. This is due to the coupling action from gyroscopic forces, arising due to the tip rotor, which have a significant effect on the response. This shows the action of gyroscopic control in addition to ply angle tailoring and active piezo control.

Fig. 18 shows the effect of taper on tip response, for $\beta_o=30^\circ$, $\theta=30^\circ$, $\Omega=400$, $\overline{\Omega}=40\,\mathrm{rad/s}$ and step forcing. As expected, the response increases with taper, i.e., a uniform cross-section beam has the lowest response, due to its bending rigidity being uniformly higher over the span. However, the attenuation rate also increases with taper, resulting in comparable settling times for all taper values. The marginal increase in period, i.e., decrease in fundamental frequency, as taper ratio increases, conforms with the result in Fig. 6. When mass of tip rotor is increased, the response attenuates with

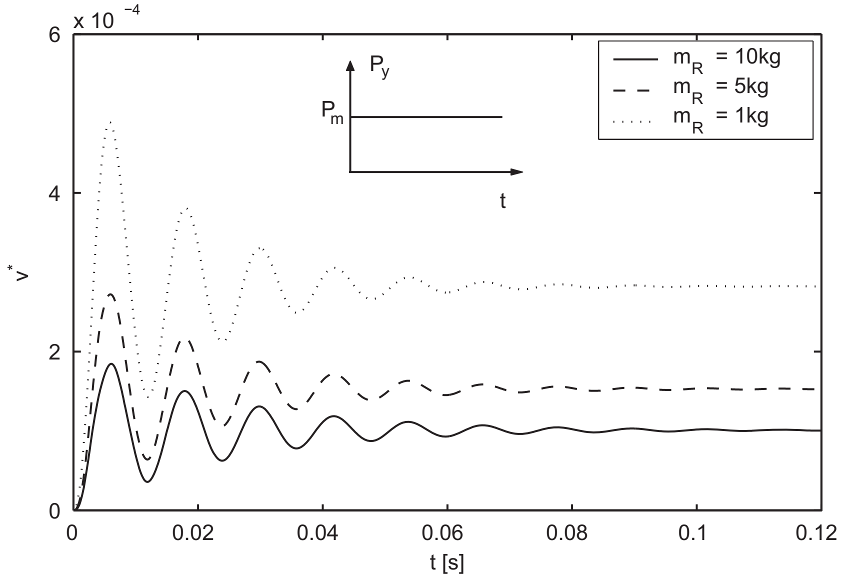

Fig. 19. Effect of tip rotor mass m_R on response v^*, step input (taper ratio $\sigma=0.25$, ply angle $\theta=30^\circ$, linear pretwist $\beta_0=60^\circ$, beam speed $\Omega=400\,\text{rad/s}$ rotor speed $\overline{\Omega}=40\,\text{rad/s}$).

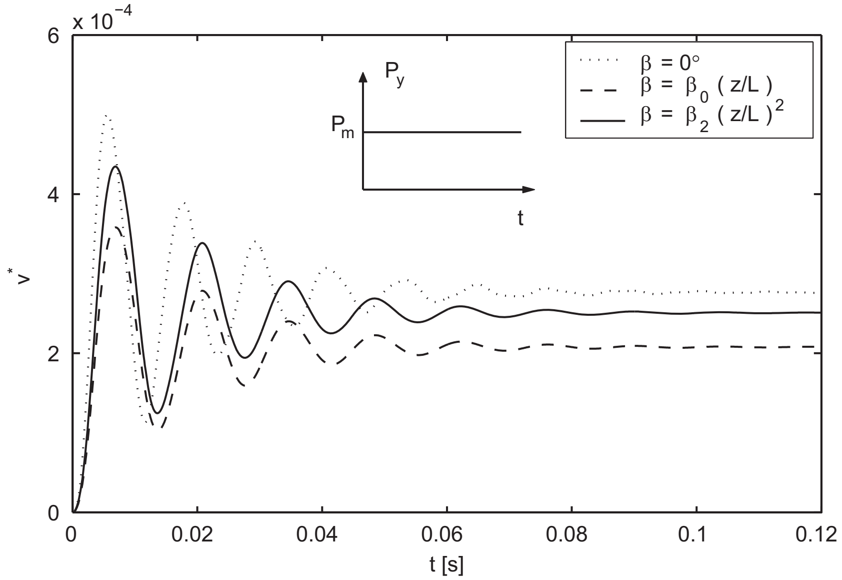

Fig. 20. Effect of pretwist on response v^* (rotor mass m_R=1 kg, taper ratio $\sigma=1$, ply angle $\theta=30^\circ$, pretwist $\beta_0=\beta_2=30^\circ$, beam speed $\Omega=400\,\text{rad/s}$, rotor speed $\overline{\Omega}=40\,\text{rad/s}$).

period visibly unchanged, as shown in Fig. 19. The data used are $\beta_0=60^\circ$, $\theta=30^\circ$, $\Omega=400$, $\overline{\Omega}=40\,\text{rad/s}$. The attenuation occurs due to centrifugal stiffening, caused by increase in rotor mass, which is more pronounced than the gyroscopic softening that occurs only for relatively small values of rotor mass as noted earlier (see Fig. 7). However, settling times are almost same for the range of rotor mass considered, since higher decay rates compensate for larger response as rotor mass decreases.

Fig. 20 shows the comparison between an untwisted, linearly pretwisted, and parabolically pretwisted beam. The data used are $\sigma=1$, $\theta=30^\circ$, pretwist $\beta_0=\beta_2=30^\circ$, $\Omega=400$, $\overline{\Omega}=40\,\text{rad/s}$. The attenuation is greatest for the beam with linear pretwist and least for the untwisted beam. Steady state responses for the linearly pretwisted and the parabolically pretwisted beams are around 82 and 94 percent that of the untwisted beam, respectively. This shows that pretwist, included from fluid dynamic considerations to enhance performance, can also be beneficially exploited for control. An increase in period, and marginal reduction in settling time, occurs for the pretwisted beams when compared to the

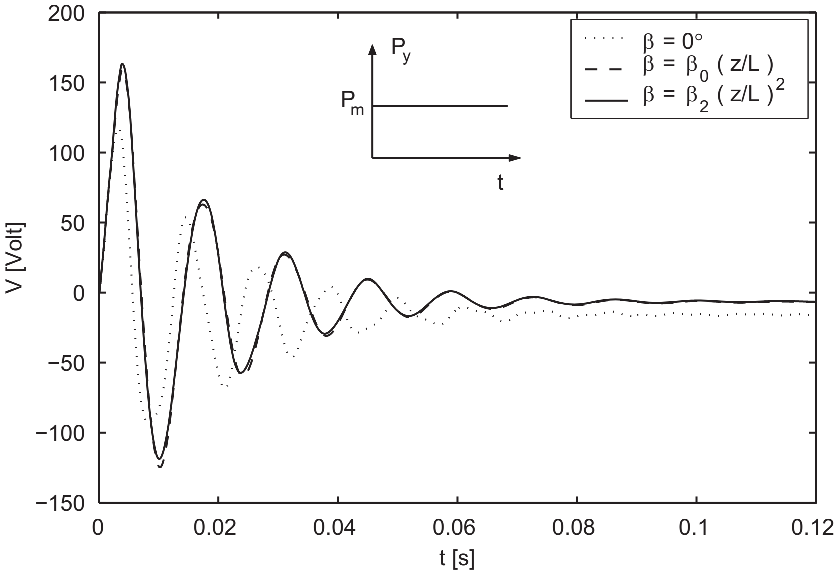

Fig. 21. Effect of pretwist on control voltage *V* (data as in Fig. 20).

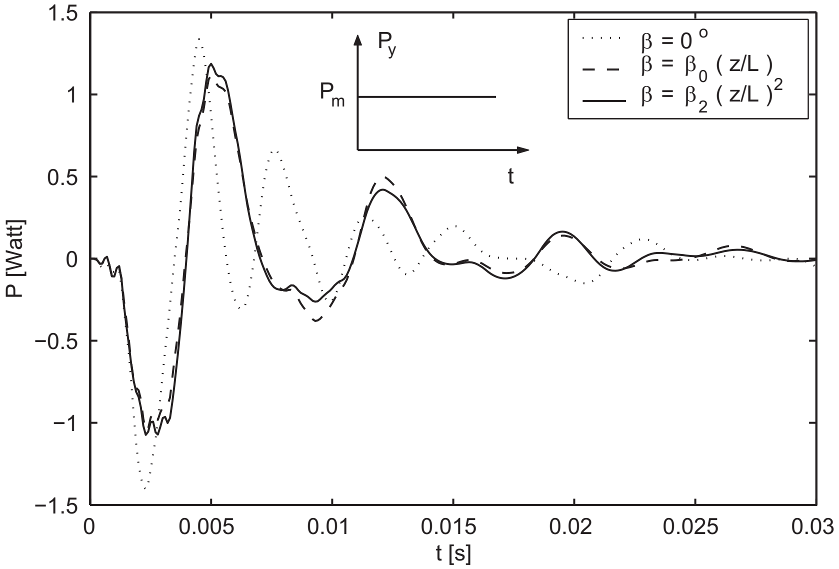

Fig. 22. Effect of pretwist on power required *P* (data as in Fig. 20).

untwisted case. The periods as well as settling times of both pretwisted beams are near identical. Both pretwisted beams have near identical requirements of control voltage and power, as seen from Figs. 21 and 22, with peak control voltage being around 23 percent higher and peak power being around 14 percent lower than for the untwisted beam. However, average voltage and power requirements in all three cases is comparable.

5. Conclusions

A structural model for a rotating, doubly tapered, pretwisted, composite blade, with piezoelectric sensors–actuator pairs, and a tip rotor has been developed based on a higher-order shear deformation theory. The optimal control problem is studied for a wide range of excitations. The variation of the electric field along the span has been considered. Thus a coupled electromechanical system is obtained, as opposed to when a uniform field is considered. This results in increased attenuation, and reduced settling time and control voltage required, i.e., the control is much better than obtained by using the previous model [18] based on a uniform electric field (Figs. 11–14). This conforms to the result reported in [20]. Peak power requirement is much lower when actuator saturation is considered, with only a modest reduction in peak response attenuation (Figs. 15 and 16). Structural tailoring studies reveal that the coupling action of gyroscopic forces due to tip rotor have a significant effect on response attenuation (Figs. 13, and17). As the tip rotor mass is increased, centrifugal stiffening dominates the gyroscopic softening behavior (Figs. 7 and 19). Parametric studies show that the HSDT provides conservative eigenfrequencies (Fig. 9). The results underscore the importance of synthesizing active control and structural tailoring, and considering through-thickness variations of shear strains and spanwise variations of electric field in achieving control effective designs. Since all states are usually not available for feedback, future work will be based on feedback of optimally estimated states, i.e., LQG control.

Acknowledgement and dedication

The financial support provided by the R&D office of IIT Bombay under project grant 05IR025 is gratefully acknowledged. This paper is dedicated to the ever-inspiring memory of Professor Liviu I. Librescu – teacher, guide, collaborator, and friend – who introduced the author to thin-walled composite rotating beams.

Appendix A. Global piezoelectric coefficients

The reduced constitutive law for the transversely isotropic piezopatch is:
Converse piezoelectric effect:

$$\begin{Bmatrix}\sigma_{ss}^P\\ \sigma_{zz}^P\\ \tau_{sz}^P\end{Bmatrix}=\begin{bmatrix}Q_{11}^P & Q_{12}^P & Q_{16}^P\\ Q_{12}^P & Q_{22}^P & Q_{26}^P\\ Q_{16}^P & Q_{26}^P & Q_{66}^P\end{bmatrix}\begin{Bmatrix}\varepsilon_{ss}\\ \varepsilon_{zz}\\ \gamma_{sz}\end{Bmatrix}-\begin{bmatrix}0 & 0 & \mathcal{E}_{31}\\ 0 & 0 & \mathcal{E}_{31}\\ 0 & 0 & 0\end{bmatrix}\begin{Bmatrix}0\\ E_2\\ E_3\end{Bmatrix} \tag{A.1}$$

$$\begin{Bmatrix}\tau_{nz}^P\\ \tau_{ns}^P\end{Bmatrix}=\begin{bmatrix}Q_{44}^P & Q_{45}^P\\ Q_{45}^P & Q_{55}^P\end{bmatrix}\begin{Bmatrix}\gamma_{nz}\\ \gamma_{ns}\end{Bmatrix}-\begin{bmatrix}\mathcal{E}_{15} & 0\\ 0 & 0\end{bmatrix}\begin{Bmatrix}E_2\\ E_3\end{Bmatrix} \tag{A.2}$$

Direct piezoelectric effect:

$$\begin{Bmatrix}D_1\\ D_2\\ D_3\end{Bmatrix}=\begin{bmatrix}0 & 0 & 0 & \mathcal{E}_{15}\\ 0 & 0 & \mathcal{E}_{15} & 0\\ \mathcal{E}_{31} & \mathcal{E}_{31} & 0 & 0\end{bmatrix}\begin{Bmatrix}\varepsilon_{ss}\\ \varepsilon_{zz}\\ \gamma_{nz}\\ \gamma_{ns}\end{Bmatrix}+\begin{bmatrix}\xi_{11} & 0 & 0\\ 0 & \xi_{22} & 0\\ 0 & 0 & \zeta_{33}\end{bmatrix}\begin{Bmatrix}0\\ E_2\\ E_3\end{Bmatrix} \tag{A.3}$$

Here D_i is the electric displacement vector and E_i is the applied electric field. The quantities ξ_{ij}, Q_{ij}^P, $\mathcal{E}_{ij}$, ζ_{ij}, denote dielectric, reduced elastic, reduced piezoelectric, and reduced dielectric constants, respectively, for the piezopatch as defined in [18] (e.g., $Q_{16}^P = Q_{26}^P = Q_{45}^P = 0$, $\mathcal{E}_{15}=e_{15}$). The transformed reduced stiffness and reduced piezoelectric coefficients for the composite beam are

$$\overline{Q}_{ij}=\overline{Q}_{ij}^H+\left(Q_{ij}^P-\overline{Q}_{ij}^H\right)f_sf_nf_z,\quad \overline{\mathcal{E}}_{ij}=\mathcal{E}_{ij}\mathcal{A}_sf_nf_z \tag{A.4}$$

where $\overline{Q}_{ij}^H$ are the transformed reduced stiffnesses of the generally orthotropic host [18].

The global piezoelectric coefficients are (see also [18])

$$L_{P22}=\oint L_{22}\,\mathrm{d}s,\quad L_{P33}=\oint L_{33}\,\mathrm{d}s,\quad a_{P10}=\oint\left(h^2/4-t_p^2\right)\mathcal{A}_sf_z\,\mathrm{d}s \tag{A.5}$$

Appendix B. Details of system discretization

EGM illustration: Consider the axial force natural BC at the tip, given by

$$\underline{\underline{\delta w_o}}:\quad a_{11}^p w_0' + \tilde{a}_{17}^p\phi' - a_{P1}\psi_o + m_R\ddot{w}_o - m_R\Omega^2(R_0+L+r_m+w_o)=0 \tag{B.1}$$

Following the EGM procedure in Section 2.5, the contribution from Eqs. (18) and (B1) to the minimization of the functional/residual is $\int_{t_0}^{t_1}\left[\int_0^L \text{Eq. (18)}\ \delta w_o\,\mathrm{d}z - \text{Eq. (B.1)}\delta w_o\right]\mathrm{d}t=0$. After suitable integration, the functional minimization becomes

$$\int_{t_0}^{t_1}\left[\int_0^L\left(\frac{b_1}{2}\delta\left\{\dot{w}_o^2+\Omega^2(R_o+z+w_o)^2\right\}-\{a_{11}^p w_0' + \tilde{a}_{17}^p\phi' - a_{P1}\psi_o\}\delta w_0'\right)\mathrm{d}z+\frac{m_R}{2}\delta\left\{\dot{w}_o^2+\Omega^2(R_o+L+r_m+w_o)^2\right\}_{z=L}\right]\mathrm{d}t=0 \tag{B.2}$$

In Eq. (B.2), terms with b_1 and m_R are components of beam- and rotor-kinetic energy, respectively, and the $\delta w_0'$ terms are components of strain energy and electrical work. Substituting approximate solution Eq. (21) in Eq. (B.2), performing the variation as $\delta(\mathbf{\Phi}_\mathbf{i}^\mathrm{T}[z]\mathbf{q}_\mathbf{i}[t])=\mathbf{\Phi}_\mathbf{i}^\mathrm{T}[z]\delta\mathbf{q}_\mathbf{i}[t]$, and integrating over the span yields the contributions to system matrices.

Mass matrix (symmetric):

$$\mathbf{M}|_{6N\times 6N} = \int_0^L [\mathbf{M_{ij}}|_{N\times N}]\,\mathrm{d}z + [\mathbf{m_{ij}}|_{N\times N}]\Big|_{z=L} \tag{B.3}$$

$\mathbf{M_{ij}} = \mathbf{m_{ij}} = \mathbf{0}$, $i \neq j$, except for $\mathbf{M_{12}}$, $\mathbf{M_{14}}$, $\mathbf{M_{15}}$, $\mathbf{M_{24}}$, $\mathbf{M_{25}}$, $\mathbf{m_{15}}$, $\mathbf{m_{24}}$; $\mathbf{m_{ii}} = m_R \boldsymbol{\Phi}_\mathbf{i} \boldsymbol{\Phi}_\mathbf{i}^\mathbf{T}$, $i = 1,2,3$; $\mathbf{m_{ii}} = I_{xxyy} \boldsymbol{\Phi}_\mathbf{i} \boldsymbol{\Phi}_\mathbf{i}^\mathbf{T}, i = 4,5$; $I_{xxyy} = m_R(r_m^2 + k_R^2/4)$; $\mathbf{m_{ii}} = I_{zz} \boldsymbol{\Phi}_\mathbf{i} \boldsymbol{\Phi}_\mathbf{i}^\mathbf{T}, i = 6$; $I_{zz} = m_R k_R^2/2$; $\mathbf{m_{ij}} = -m_R r_m \boldsymbol{\Phi}_\mathbf{i} \boldsymbol{\Phi}_\mathbf{j}^\mathbf{T}, i \neq j$;

Gyroscopic matrix (skew symmetric):

$$\mathbf{G} = [\mathbf{G_{ij}}]|_{z=L}, \quad \mathbf{G_{ij}} = \mathbf{0} \text{ except for } \mathbf{G_{45}} = -2\overline{\Omega} I_{zz} \boldsymbol{\Phi}_\mathbf{4} \boldsymbol{\Phi}_\mathbf{5}^\mathbf{T}, \quad \mathbf{G_{54}} = 2\overline{\Omega} I_{zz} \boldsymbol{\Phi}_\mathbf{5} \boldsymbol{\Phi}_\mathbf{4}^\mathbf{T} \tag{B.4}$$

References

[1] C. Kim, S.R. White, Thick-walled composite beam theory including 3-D elastic effects and torsional warping, *International Journal of Solids and Structures* 34 (1997) 4237–4259.

[2] A. Rosen, R.G. Loewy, M.B. Mathew, Use of twisted principal coordinates and non-physical coordinates in blade analysis, *Vertica* 11 (1987) 541–572.

[3] S.N. Jung, V.T. Nagaraj, I. Chopra, Refined structural dynamics model for composite rotor blades, *AIAA Journal* 39 (2001) 339–348.

[4] O. Song, L. Librescu, S.Y. Oh, Vibration of pretwisted adaptive rotating blades modeled as anisotropic thin-walled beams, *AIAA Journal* 39 (2001) 285–295.

[5] H.H. Yoo, J.Y. Kwak, J. Chung, Vibration analysis of rotating pre-twisted blades with a concentrated mass, *Journal of Sound and Vibration* 240 (2001) 891–908.

[6] J.R. Banerjee, H. Su, D.R. Jackson, Free vibration of rotating tapered beams using the dynamic stiffness method, *Journal of Sound and Vibration* 298 (2006) 1034–1054.

[7] S.A. Fazelzadeh, M. Hosseini, Aerothermoelastic behavior of supersonic rotating thin-walled beams made of functionally graded materials, *Journal of Fluids and Structures* 23 (2007) 1251–1264.

[8] S.A. Fazelzadeh, P. Malekzadeh, P. Zahedinejad, M. Hosseini, Vibration analysis of functionally graded thin-walled rotating blades under high temperature supersonic flow using the differential quadrature method, *Journal of Sound and Vibration* 306 (2007) 333–348.

[9] S.Y. Lee, J.J. Sheu, S.M. Lin, In-plane vibrational analysis of a rotating curved beam with elastically restrained root, *Journal of Sound and Vibration* 315 (2008) 1086–1102.

[10] S.Y. Lee, S.M. Lin, Y.S. Lin, Instability and vibration of a rotating Timoshenko beam with precone, *International Journal of Mechanical Sciences* 51 (2009) 114–121.

[11] C. Mei, Application of differential transformation technique to free vibration analysis of a centrifugally stiffened beam, *Computers and Structures* 86 (2008) 1280–1284.

[12] D.L. Kunz, Multimode control of a rotating uniform cantilever beam, *AIAA Journal* 25 (2002) 193–199.

[13] S.C. Choi, J.S. Park, J.H. Kim, Active damping of rotating composite thin-walled beams using MFC actuators and PVDF sensors, *Composite Structures* 76 (2006) 362–374.

[14] S.C. Choi, J.S. Park, J.H. Kim, Vibration control of pretwisted rotating composite thin-walled beams with piezoelectric fiber composites, *Journal of Sound and Vibration* 300 (2007) 176–196.

[15] K. Wei, G. Meng, S. Zhou, J. Liu, Vibration control of variable speed/acceleration rotating beams using smart materials, *Journal of Sound and Vibration* 298 (2006) 1150–1158.

[16] G.P. Cai, C.W. Lim, Active control of a flexible hub-beam system using optimal tracking control method, *International Journal of Mechanical Sciences* 48 (2006) 1150–1162.

[17] G.P. Cai, C.W. Lim, Dynamics studies of a flexible hub-beam system with significant damping effect, *Journal of Sound and Vibration* 318 (2008) 1–17.

[18] C.D. Shete, N.K. Chandiramani, L.I. Librescu, Optimal control of a pretwisted shearable smart composite rotating beam, *Acta Mechanica* 191 (2007) 37–58.

[19] S.M. Lin, PD control of a rotating smart beam with an elastic root, *Journal of Sound and Vibration* 312 (2008) 109–124.

[20] M. Pietrzakowski, Piezoelectric control of composite plate vibration: effect of electric potential distribution, *Computers and Structures* 86 (2008) 948–954.

[21] S. Narayanan, V. Balamurugan, Fiinite element modelling of piezolaminated smart structures for active vibration control with distributed sensors and actuators, *Journal of Sound and Vibration* 262 (2003) 529–562.

[22] C.M.A. Vasquez, J. Dias Rodrigues, Active vibration control of smart piezoelectric beams: comparison of classical and optimal feedback control strategies, *Computers and Structures* 84 (2006) 1402–1414.

[23] N.W. Hagood, A. von Flotow, Damping of structural vibrations with piezoelectric materials and passive electrical networks, *Journal of Sound and Vibration* 146 (1991) 243–268.

[24] U. Andreaus, F. Dell'Isola, M. Porfiri, Piezoelectric passive distributed controllers for beam flexural vibrations, *Journal of Vibration and Control* 10 (2004) 625–659.

[25] S.O.R. Moheimani, A.J. Fleming, *Piezoelectric Transducers for Vibration Control and Damping*, Springer, London, 2006.

[26] D. Guyomar, C. Richard, S. Mohammadi, Damping behavior of semi-passive vibration control using shunted piezoelectric materials, *Journal of Intelligent Material Systems and Structures* 19 (2008) 977–985.

[27] J.H. Han, I. Lee, Optimal placement of piezoelectric sensors and actuators for vibration control of a composite plate using genetic algorithms, *Smart Materials and Structures* 8 (1999) 257–267.

[28] K.D. Dhuri, P. Seshu, Multi-objective optimization of piezo actuator placement and sizing using genetic algorithm, *Journal of Sound and Vibration* 323 (2009) 495–514.

[29] L. Librescu, O. Song, C.A. Rogers, Adaptive vibrational behavior of cantilevered structures modeled as composite thin-walled beams, *International Journal of Engineering Science* 31 (1993) 775–792.

[30] C. Maurini, J. Pouget, F. dell'Isola, On a model of layered piezoelectric beams including transverse stress effect, *International Journal of Solids and Structures* 41 (2004) 4473–4502.

[31] H.S. Tzou, *Piezoelectric Shells—Distributed Sensing and Control of Continua*, Kluwer, Dordrecht, 1993.

[32] D.J. Ewins, R. Henry, Structural dynamic characteristics of individual blades. *Vibration and rotordynamics—Lecture Series* 1992-06, AGARDograph no. 298, Paper 14, Von Karman Institute for Fluid Mechanics, Belgium, 1992, pp. 14.1–27.

[33] G.J. Simitses, *Introduction to the Elastic Stability of Structures*, Prentice-Hall, New Jersey, 1976.

[34] L. Meirovitch, *Principles and Techniques of Vibrations*, Prentice-Hall, New Jersey, 1997.

[35] M. Porfiri, C. Maurini, J. Pouget, Identification of electromechanical modal parameters of linear piezoelectric structures, *Smart Materials and Structures* 16 (2007) 323–331.

[36] J.E. Potter, Matrix quadratic solutions, *SIAM Journal of Applied Mathematics* 14 (1966) 496–501.

[37] W.K. Gawronski, *Dynamics and Control of Structures—A Modal Approach*, Springer, New York, 1998.

[38] C. Maurini, M. Porfiri, J. Pouget, Numerical methods for modal analysis of stepped piezoelectric beams, *Journal of Sound and Vibration* 298 (2006) 918–933.
[39] N.D. Maxwell, S.F. Asokanathan, Modal characteristics of a flexible beam with multiple distributed actuators, *Journal of Sound and Vibration* 269 (2004) 19–31.
[40] S. Na, L. Librescu, Optimal vibration control of thin-walled anisotropic cantilevers exposed to blast loading, *Journal of Guidance, Control, and Dynamics* 23 (2000) 491–500.
[41] T. Yokohama, M. Markiewicz, Flexural vibrations of a rotating Timoshnko beam with tip mass, *AIAA-Pacific Vibration Conference*, Kitakyushu, Japan, November 1993.
[42] A.D. Wright, C.E. Smith, R.W. Thresher, J.L.C. Wang, Vibration modes of centrifugally stiffened beams, *Journal of Applied Mechanics* 49 (1982) 197–202.
[43] H.P. Lee, Vibration of an inclined rotating cantilever beam with tip mass, *Journal of Vibration and Acoustics* 115 (1993) 241–245.